



1 **High-precision atmospheric oxygen measurement comparisons between a newly built**  
2 **CRDS analyzer and existing measurement techniques**

3

4 Tesfaye A. Berhanu<sup>1,2</sup>, John Hoffnagle<sup>2</sup>, Chris Rella<sup>2</sup>, David Kimhak<sup>2</sup>, Peter Nyfeler<sup>1</sup>, Markus  
5 Leuenberger<sup>1</sup>

6 <sup>1</sup>*Climate and Environmental Physics, Physics Institute and Oeschger Centre for Climate Change Research,*  
7 *University of Bern, Bern, Switzerland*

8 <sup>2</sup>*Picarro Inc., 3105 Patrick Henry Drive, Santa Clara, CA, USA*

9

10 **Abstract**

11 Carbon dioxide and oxygen are tightly coupled in land-biospheres CO<sub>2</sub> - O<sub>2</sub> exchange  
12 processes, while they are not coupled in oceanic exchange. For this reason, atmospheric  
13 oxygen measurements can be used to constrain the global carbon cycle, especially oceanic  
14 uptake. However, accurately quantifying the small (~1-100 ppm) variations in O<sub>2</sub> is  
15 analytically challenging due to the very large atmospheric background which constitutes  
16 about 20.9 % (~209500 ppm) of atmospheric air. Here we present comprehensive laboratory  
17 and field studies for a newly developed high-precision oxygen mixing ratio and isotopic  
18 composition analyzer (Picarro G-2207) that is based on cavity ring-down spectroscopy  
19 (CRDS). From the laboratory tests, we have calculated a short-term precision (standard error  
20 of one-minute measurements) of < 1 ppm for this analyzer based on measurements of eight  
21 standard gases analyzed for two hours consecutively. In contrast to the currently existing  
22 techniques, the instrument has an excellent long-term stability and therefore a calibration  
23 every 12 hours is sufficient to get an overall uncertainty of < 5 ppm. Measurements of  
24 ambient air were also conducted at the High-Altitude Research Station, Jungfrauoch and the



25 Beromünster tall tower in Switzerland. At both sites, we observed opposing and diurnally  
26 varying CO<sub>2</sub> and O<sub>2</sub> profiles due to different processes such as combustion, photosynthesis  
27 and respiration. Based on the combined measurements at Beromünster tower, we determined  
28 height dependent O<sub>2</sub>:CO<sub>2</sub> oxidation ratios varying between -0.98 to -1.60, which increase  
29 with the height of the tower inlet, possibly due to different source contribution such as natural  
30 gas combustion with high oxidation ratio and biological processes which are at the lower end.

### 31 **1. Introduction**

32 Atmospheric oxygen comprises about 20.9 % of the global atmosphere and in the past  
33 decade its concentration decreased at a rate of ~ 20 per meg yr<sup>-1</sup> (Keeling and Manning, 2014)  
34 mainly associated with the increase in fossil fuel combustion. In contrast, the global average  
35 atmospheric CO<sub>2</sub> mixing ratio increased to 402.8 ppm averaged over 2016 (predicted to grow  
36 by 2 % in 2017) since its preindustrial value of 280 ppm (Le Quéré et al., 2017). As the  
37 variability of atmospheric oxygen is directly linked to the carbon cycle, both its short and  
38 long-term observations can be used to better constrain the carbon cycle. For example, since  
39 first suggested by Keeling and Shertz (1992) the long-term trends derived from concurrent  
40 measurements of atmospheric CO<sub>2</sub> and O<sub>2</sub> have been widely used to quantify the partitioning  
41 of atmospheric CO<sub>2</sub> between the land-biosphere and oceanic sinks (Battle et al., 2000; Goto et  
42 al., 2017; Manning and Keeling, 2006; Valentino et al., 2008). This method hinges on the  
43 linear coupling between CO<sub>2</sub> and O<sub>2</sub> with an oxidation ratio (OR) of 1.1 for the terrestrial  
44 biosphere photosynthesis-respiration processes ( $\alpha_b$ ) and 1.4 for fossil fuel combustion ( $\alpha_f$ )  
45 while they are decoupled for oceanic processes. Meanwhile, the short-term variability in  
46 atmospheric oxygen can be used to estimate marine biological productivity and air-sea gas  
47 exchange (Keeling et al., 1998; Nevison et al., 2012). However, the accuracy of these  
48 estimates is primarily linked to the accuracy and precision of atmospheric O<sub>2</sub> measurements



49 and the assumed ORs for the different processes which are highly variable in contrast to  
50 atmospheric CO<sub>2</sub> that can be well measured within the precision guidelines set by the Global  
51 Atmospheric Watch (GAW) ( $\pm 0.1$  ppm for the northern hemisphere).

52         Currently there are several techniques that can measure atmospheric O<sub>2</sub> variations as  
53 oxygen concentration based on interferometric, paramagnetic, UV absorption and fuel cell  
54 technology (Keeling, 1988a; Manning et al., 1999; Stephens et al., 2007) or as O<sub>2</sub>/N<sub>2</sub> ratios to  
55 account for the large background effect using Gas chromatography with thermal conductivity  
56 detector (GC-TCD) or Gas chromatography coupled to mass spectrometry (GC-MS) (Bender  
57 et al., 1994; Tohjima, 2000). Despite the fact that these techniques have been commercially  
58 available for more than two decades, accurate quantification of atmospheric oxygen  
59 variability remains challenging primarily because the small ppm-level atmospheric oxygen  
60 signal rides on a  $\sim 210,000$  ppm background, which places stringent requirements on the  
61 precision and drift of the analysis methods. The techniques listed above struggle to routinely  
62 achieve the necessary performance for various reasons, including i) instability over time that  
63 requires frequent measurement interruption for calibration, ii) measurement bias with ambient  
64 and sample temperature and/or pressure, and/or iii) systematic errors in the measurement due  
65 to other atmospheric species. Further, some techniques require the use of consumables and  
66 rely on high vacuum, which complicates field deployment.

67         In this manuscript we describe a new high precision oxygen concentration and isotopic  
68 composition analyzer by Picarro Inc., Santa Clara, USA (G-2207) based on CRDS  
69 technology. Here, we will introduce the analyzer design principles in details, describe the  
70 unique features of the analyzer and evaluate its performance based on various independent  
71 laboratory and field tests by comparing it with currently existing techniques. Then, we will



72 present and interpret our observations based on field measurements. Finally, we will conclude  
73 its overall performance and provide recommendations and possible improvements.

## 74 **2. Analyzer design principles**

75 The analyzer described here is derived from the Picarro G2000 series of CRDS  
76 analyzers. The basic elements have been described elsewhere (Crosson, 2008; Martin et al.,  
77 2016; Steig et al., 2014): briefly, the instrument is built around a high-finesse, traveling-wave  
78 optical cavity, which is coupled to either of two single-frequency DFB-stabilized  
79 semiconductor lasers. One cavity mirror is mounted on a piezoelectric translator (PZT) to  
80 allow fine tuning of the cavity resonance frequencies. A semiconductor optical amplifier  
81 between the laser sources and the cavity boosts the laser power and serves as a fast-optical  
82 switch. The cavity body is constructed of invar and enclosed in a temperature stabilized box  
83 ( $T = 45^{\circ}\text{C}$ , stabilized to approximately  $0.01^{\circ}\text{C}$ ) for dimensional and spectroscopic stability.  
84 A vacuum pump pulls the gas to be sampled through the cavity and a proportional valve  
85 between the cavity and the pump maintains the sample pressure in the cavity at a value of 340  
86 hPa, with variations on the order of 1 Pa. The instrument has a wavelength monitor, based  
87 upon measurements of interference fringes from a solid etalon, which is used to control the  
88 laser wavelength by adjusting the laser temperature and current. A high-speed photodiode  
89 monitors the optical power emerging from the cavity. The instrument's data acquisition  
90 system sweeps the laser frequency over the spectral feature to be measured, modulates the  
91 laser output to initiate ring-downs, and fits the ring-down signal to an exponential function to  
92 generate a spectrogram of optical loss versus laser frequency. Subsequent program modules  
93 compare the measured loss spectrum to a spectral model, using non-linear least-squares fitting  
94 (Press et al., 1986) to find the best-fit model parameters and thereby obtain a quantitative  
95 measure of the absorption due to the target molecule, and finally apply a calibration factor to



96 the optical absorption to deduce the molecular concentration. When operating in its normal  
97 gas analysis mode, the instrument acquires about 200-300 ring-downs per second and  
98 achieves a noise equivalent absorption of typically about  $10^{-11} \text{ cm}^{-1} \text{ Hz}^{-1/2}$ , with some variation  
99 between instruments.

100 The primary goal when designing this analyzer was to measure the molecular oxygen  
101 concentration with few-per-meg level precision and stability. In this context operational  
102 stability is as important as signal-to-noise. Our experience has been that the most stable  
103 operation of the analyzer is achieved when the optical phase length of the cavity is held as  
104 nearly constant as possible. In this case the free spectral range (FSR) of the temperature  
105 stabilized, invar ring-down cavity provides a better optical frequency standard than the etalon-  
106 based wavelength monitor, which in turn allows more consistent measurements of absorption  
107 line width and integrated absorption line intensity (Steig et al., 2014). For a small, field-  
108 deployable instrument, it is not practical to stabilize the absolute frequencies of the cavity  
109 modes to an optical frequency standard (Hodges et al., 2004) but the oxygen lines themselves,  
110 under conditions of constant temperature and pressure, provide an adequate frequency  
111 reference. The oxygen spectrum was also used to calibrate the FSR, by comparing a wide  
112 (approximately  $10 \text{ cm}^{-1}$ ) FSR-spaced spectrum with the Hitran database (Rothman et al.,  
113 2013).

114 To determine molecular oxygen concentration, the analyzer measures absorption of the  
115 Q13Q13 component of the  $a^1\Delta_g \leftarrow X^3\Sigma_g^-$  band, at a frequency of  $7878.805547 \text{ cm}^{-1}$ ,  
116 according to the latest edition of Hitran (Gordon et al., 2017). This is one of the strongest  
117 near-infrared lines of oxygen, well separated from other oxygen lines, and reasonably free of  
118 spectral interference from water, carbon dioxide, methane, and other constituents of clean air.  
119 The spectral model for this line was developed using reference spectra of clean, dry, synthetic



120 air that were acquired with the same hardware as in the field-deployable analyzer, but with  
121 special-purpose software that allows it to operate as a more general spectrometer.

122         Recently, considerable work has been done to advance the understanding of spectral  
123 line shapes and to define functional representations that better describe the processes that  
124 determine spectral line shapes than does the Voigt model (Hartmann et al., 2008; Tennyson et  
125 al., 2014). Line shape studies have been published for the 1.27  $\mu\text{m}$  band of  $\text{O}_2$  (Fleisher et al.,  
126 2015; Lamouroux et al., 2014), though not to our knowledge for the Q branch. The apparatus  
127 used here is not capable of spectroscopic studies of comparable precision; the absolute  
128 temperature and pressure monitoring and especially the frequency metrology are far too crude  
129 for that purpose. Our goal is merely to define a simple model of the Q13Q13 line that is  
130 adequate for least-squares retrievals of the  $\text{O}_2$  absorption under the limited range of conditions  
131 (stabilized temperature and pressure) that the operational analyzer experiences in the field.  
132 The CRDS analyzers use the Galatry function (Varghese and Hanson, 1984), which is  
133 distinctly better than the Voigt and still easily and quickly evaluated for line shape modeling.  
134 Ultimately, the usefulness of the spectral model is to be evaluated by the precision and  
135 stability of the  $\text{O}_2$  measurements when compared with established techniques. We also note at  
136 this point that Sironneau, Fleisher, and Hodges have made detailed measurements of lines in  
137 the R branch of the  $a^1\Delta_g \leftarrow X^3\Sigma_g^-$  band and observed departures from simple, linear  
138 absorption, which they interpret as arising from collision-induced absorption (Fleisher et al.,  
139 2015). This has two important consequences for  $\text{O}_2$  monitoring: the line strength is not  
140 independent of sample pressure, and optical absorption is not linear in laser intensity. We do  
141 not expect these effects to be too severe for our application because the ring-down cavity is  
142 stabilized to a very narrow range of temperature and pressure. In addition, the optical power  
143 in the ringdown cavity set by the ring-down detector threshold, which is used to trigger the



144 laser shutoff and subsequent ring-down waveform acquisition. The fact that all ring-downs  
145 occur at the same intracavity power should minimize the effect of collision-induced  
146 absorption. We have observed some excess noise on the ring-down time constants for the  
147 highest loss points at the peak of the Q13Q13 line, which might have to do with the fitting of  
148 the ring-down signal if absorption is not linear, but we cannot be certain of this explanation at  
149 present.

150 For spectral model development, this spectrometer has the drawback that the cavity  
151 FSR, equal to about  $0.0206 \text{ cm}^{-1}$ , is too large to reveal much detail of the absorption line  
152 shape, even with the simplifying assumption of a Galatry line shape. We therefore acquired a  
153 set of four interleaved spectra, with the PZT-actuated mirror moved to offset the cavity modes  
154 of the individual FSR-spaced spectra by one-fourth of an FSR. The precise offsets were  
155 determined from fits to the strong and well-isolated  $\text{O}_2$  lines in the spectra. From the  
156 consistency of the fitted line centers, we estimate that the positioning of the interleaved  
157 spectra was accurate to approximately 10 MHz. The spectrum of the Q13Q13 line acquired in  
158 this manner is shown in Figure 1, together with the best-fit Galatry function. It stands out that  
159 the residuals that are largely an odd function of detuning from the line center: this shows the  
160 limitations of the Galatry model in this case, since the Galatry function is purely even about  
161 the line center. The shape of the absorption line in this model is specified by two  
162 dimensionless parameters: the collisional broadening parameter

$$163 \quad \gamma = \gamma / \sigma_D \quad (1)$$

164 and the collisional narrowing parameter

$$165 \quad z = \beta / \sigma_D \quad (2)$$

166 where  $\gamma$  is the frequency of broadening transitions,  $\beta$  is the frequency of narrowing collisions,  
167 and  $\sigma_D$  is the Doppler width of the transition, given by



$$168 \quad \sigma_D = \nu_0(2k_B T/Mc^2)^{1/2} \quad (3)$$

169 where  $\nu_0$  is the transition frequency,  $k_B$  is Boltzmann's constant,  $T$  is the sample temperature,  
170  $M$  is the molecular mass, and  $c$  is the speed of light. Figure 2 shows the values of  $y$  and  $z$   
171 obtained from spectra acquired in the same way as Figure 1, as a function of cavity pressure.  
172 The values depend linearly on pressure, as expected from the Galatry model, but the  
173 unconstrained linear fits do not go precisely through the origin. It is not clear whether this  
174 represents a breakdown of the Galatry model or simply reflects the limited quality of the data  
175 set. The slope of  $y$  can be converted to an air-broadened collisional width  $\gamma_{\text{air}} = 0.0442 \text{ cm}^{-1}$   
176  $^1/\text{atm}$ , which agrees with the Hitran value of  $0.0460 \text{ cm}^{-1}/\text{atm}$  (Rothman et al., 2013) to within  
177 the uncertainty estimate stated by Hitran. The slope of  $z$  can be interpreted in terms of the  
178 optical diffusion coefficient (Fleisher et al., 2015), yielding  $D = 0.285 \text{ cm}^2 \text{ s}^{-1}$ , compared to  
179 the literature value of  $0.233 \text{ cm}^2 \text{ s}^{-1}$  for  $\text{O}_2$  in air at  $45 \text{ }^\circ\text{C}$  (Marrero and Mason, 1972).  
180 Although the anticipated use of the analyzer is for ambient air samples having a very small  
181 range of  $\text{O}_2$  concentrations, we did investigate the variation of the line shape in binary  
182 mixtures of  $\text{O}_2$  and  $\text{N}_2$  shown in Figure 3. The error bars are taken from the output of the  
183 Levenberg-Marquardt fitting routine (Press et al., 1992). The dependence of the collisional  
184 broadening parameter  $z$  on  $\text{O}_2$  mole fraction was considered too small to be significant, but  
185 the variation in  $y$  was used in the subsequent analysis of the air samples. Note that Wójtcwicz  
186 et al. (Wójtcwicz et al., 2014) also found collisional broadening coefficients for nitrogen to be  
187 slightly larger than for oxygen in measurements of one  $\text{O}_2$  line in the B-band.

188 The primary goal in designing the analyzer was to achieve high enough precision to  
189 make meaningful measurements of  $\text{O}_2$  in clean atmospheric samples. Although the current  
190 best practice for such high-precision measurements is to work with dried samples, we decided





191 to include high precision measurements of water vapor. There were two reasons for this  
192 decision: one is to serve as a monitor for residual water vapor, which is difficult to remove  
193 completely from the ring-down cavity and associated sample handling hardware, and the  
194 second and more ambitious reason was to see how well the effect of water vapor could be  
195 corrected for in measurements of undried ambient air. While it was considered unlikely that  
196 measurements of undried air could compete in accuracy with those of dried air, it might be  
197 possible to correct for water vapor well enough to enable useful measurements in some  
198 circumstances without the expense and inconvenience of drying the sample. For this purpose,  
199 a second laser was added, which probes the  $7_{1,6} \rightarrow 8_{4,5}$  component of the  $2\nu_3$  band of water  
200 vapor, at a frequency of  $7816.75210 \text{ cm}^{-1}$  (Gordon et al., 2017). The Galatry model was used  
201 to fit spectra of synthetic air humidified to various levels of water vapor concentration. These  
202 fits also included two other nearby, very weak water lines, with intensities less than 1% of the  
203 strong transition, in order that their absorption should not perturb the line shape of the main  
204 transition. Results for the shape of the  $7816.75210 \text{ cm}^{-1}$  line are shown in Figure 4. At the  
205 level that we can measure, only the  $y$ -parameter has a meaningful variation with water  
206 concentration. From the linear fit one obtains a pressure broadening coefficient for air,  $\gamma_{\text{air}} =$   
207  $0.0752 \text{ cm}^{-1}/\text{atm}$ , in reasonable agreement with the Hitran value  $\gamma_{\text{air}} = 0.0787 \text{ cm}^{-1}/\text{atm}$   
208 (Gordon et al., 2017), and a self-broadening coefficient  $\gamma_{\text{self}} = 0.413 \text{ cm}^{-1}/\text{atm}$ , to be compared  
209 with the Hitran value  $\gamma_{\text{self}} = 0.366 \text{ cm}^{-1}/\text{atm}$ . Since the uncertainty estimate for the Hitran  
210 values is 10 % to 20 %, this level of agreement seems reasonable.

211 We also looked at absorption from water near the Q13Q13 absorption line of  $\text{O}_2$ .  
212 These spectra were measured in a background of pure nitrogen to reveal the very weak lines  
213 interfering with the  $\text{O}_2$  measurement. Without the strong  $\text{O}_2$  lines, it was impossible to  
214 interleave FSR-spaced spectra, so in this case the frequency axis comes from the analyzer's



215 wavelength monitor. The upper panel of Figure 5 shows the spectrum of saturated water vapor  
216 in nitrogen, together with a fit to a Voigt model of the molecular lines. The measurement was  
217 made at a pressure of 340 hPa and temperature of 45° C. The two most prominent features in  
218 this spectrum are actually the Q17R16 and Q13Q13 lines from traces of O<sub>2</sub> remaining in the  
219 sample while the other features are from water. The lower panel of Figure 5 shows the lines  
220 tabulated in Hitran. Immediately after the data in Figure 5 were acquired, measurements were  
221 also made at 7816.85210 cm<sup>-1</sup>, to establish the relationship between the absorption strengths  
222 in the two spectral regions. All the water lines that were observed, in both spectral regions, are  
223 from the dominant 161 isotopologue of water, so changes in isotopic composition of  
224 atmospheric water does not lead to variation in the relative strengths of the lines we measure.  
225 Hitran simulations for molecules other than water that are expected to be present in clean,  
226 ambient air indicate that direct interference with the Q13Q13 line should be negligible at the  
227 level of precision considered here. In the case of CO<sub>2</sub>, the dilution of oxygen due to 400 ppm  
228 of CO<sub>2</sub> is significant, and larger than any direct spectral interference.

229 Finally, we investigated the influence of water vapor on the shape of the O<sub>2</sub> Q13Q13  
230 line. Switching between the two lasers sources, we acquired FSR-spaced spectra of  
231 humidified synthetic air, alternately covering the 7817 cm<sup>-1</sup> and 7878 cm<sup>-1</sup> regions. Individual  
232 spectra were acquired in less than 2 s, so changes in water vapor concentration between  
233 spectra were small. These spectra, with frequency resolution of 0.0206 cm<sup>-1</sup>, were analyzed by  
234 nonlinear least-squares fitting with the following spectral models: the 7817 cm<sup>-1</sup> spectra were  
235 modeled as the sum of an empty-cavity baseline having an adjustable offset level and slope  
236 and three water peaks and the two weak perturbing peaks. The molecular absorption of the  
237 main peak was expressed as an adjustable amplitude, A<sub>w</sub>, multiplying a dimensionless, area-  
238 normalized Galatry function (Varghese and Hanson, 1984). The weak perturbers were



239 modeled by Voigt profiles with amplitudes and line widths that constrained to be in fixed  
240 ratios to the strong line, and therefore added no new degrees of freedom to the fitting  
241 procedure. Since the amplitude  $A_w$  multiplies an area-normalized shape function, it is  
242 essentially equivalent to the area of the absorption line, to the extent that the Galatry model  
243 provides a valid description of the line shape. The Doppler width of the Galatry function was  
244 fixed based on the measured cell temperature, the y-parameter was allowed to vary, and the z-  
245 parameter was constrained to be proportional to y, based on the earlier measurements. In  
246 addition, the center frequency of the Galatry function was adjusted to match the data set,  
247 giving a total of five free parameters for this fit. The  $7878\text{ cm}^{-1}$  spectra were modeled with an  
248 adjustable baseline offset and slope and molecular absorption amplitude,  $A_{O_2}$ , describing the  
249 Q13Q13  $O_2$  line. Here, too, the y-parameter and centration of the  $O_2$  lines were allowed to  
250 adjust, and the z-parameter was constrained to be proportional to y. The weak water lines  
251 interfering with oxygen absorption were included in the model, but with no additional free  
252 parameters, rather the amplitudes were preset based on the measured water absorption at  $7817$   
253  $\text{cm}^{-1}$  and the previously determined amplitude relationships between the water lines.  
254 Collisional broadening of the Q13Q13  $O_2$  line by water vapor is shown in Figure 6. From the  
255 linear fit one obtains a coefficient for collisional broadening of the Q13Q13 line by water  
256 vapor of  $\gamma_{\text{water}} = 0.0442\text{ cm}^{-1}/\text{atm}$ . We are not aware of previous measurements of this  
257 quantity.

258 The alternating measurements at  $7817\text{ cm}^{-1}$  and  $7878\text{ cm}^{-1}$  also calibrated the  
259 relationship between water mole fraction and the absorption at  $7817\text{ cm}^{-1}$ , using a dilution  
260 analysis described by Filges et al. (Filges et al., 2018), who showed that the results obtained  
261 this way agree well with water vapor fractions measured with a conventional hygrometer.  
262 Figure 7 shows the measured amplitudes of the water and oxygen lines for samples of variable



263 humidity. Since the air came from a tank of constant composition, the oxygen concentration  
264 changes due to dilution of oxygen when water is added. Assuming that this is the sole cause  
265 of the change in measured absorption, since the line shapes were being constantly adjusted to  
266 account for changes in collisional broadening, it is straightforward to deduce the relation  
267 between the water fraction and the absorption amplitude. This calibration was used to  
268 generate the water fraction axes in Figures 4 and 6. We note that we did not take particular  
269 care to control or measure the quantity of dissolved gases, especially oxygen and carbon  
270 dioxide, in the water used for this experiment. While these gases would not significantly  
271 affect the water calibration, they may affect the water vapor correction of the oxygen  
272 measurement at the ppm level. More work needs to be done to investigate the water vapor  
273 correction of the oxygen measurement.

274         The observations described above were used to design a method to measure oxygen  
275 concentration in ambient air. Gas from the inlet to the analyzer is drawn through the cavity at  
276 a rate of about 100 scm and the conditions in the cavity are held stable at 340 hPa and 45° C.  
277 In its analysis mode the analyzer alternately measures ring-downs in the 7817 cm<sup>-1</sup> and 7878  
278 cm<sup>-1</sup> regions. At 7878 cm<sup>-1</sup> measurements are made at 11 different frequencies, spaced by one  
279 FSR of the cavity and centered at the peak of the Q13Q13 line. Multiple ring-down  
280 measurements are made to improve the precision of the loss determination, with a total of 305  
281 ring-downs allocated to one spectrum. In the 7817 cm<sup>-1</sup> region measurements are also made  
282 at 11 distinct frequencies at FSR spacings. Only 35 ring-downs are allocated to this spectral  
283 region, since the measurement of O<sub>2</sub> is much more important than water vapor. The data sets  
284 are analysed using a Levenberg-Marquardt fitting routine, which adjusts five free parameters  
285 in each region to find the best agreement to a spectral model based on Galatry line shapes, as  
286 described above. One of the outputs of the 7878 cm<sup>-1</sup> fit is the frequency offset of the FSR



287 grid from the center of the Q13Q13 line. This information is used to adjust the position of the  
288 PZT actuated mirror to keep the measurements centered on the line, effectively stabilizing the  
289 optical path length of the cavity to the frequency of the O<sub>2</sub> line. The reported water fraction is  
290 obtained by multiplying the fitted amplitude of the water line by a calibration constant derived  
291 from the dilution experiment as explained above. For the O<sub>2</sub> fraction a slightly more  
292 complicated procedure is followed. It was observed that the least-squares fitting of the data  
293 gives highly correlated results for the amplitude of the absorption line and the line width  
294 parameter  $y$ . The correlation may be due in part to the fitting procedure itself (Press et al.,  
295 1992) and it may also have a contribution from pressure variations that the pressure sensor is  
296 unable to detect. The ratio  $A_{O_2}/y$  can be determined from the fit much more precisely than  
297  $A_{O_2}$  alone and so gives a more sensitive measurement of molecular absorption. It also has the  
298 advantage of being independent of sample pressure, to the extent that the Galatry model  
299 applies (Figure 2). However, using the ratio  $A_{O_2}/y$  as a metric for absorption adds additional  
300 complications if measurements are to be made over a range of O<sub>2</sub> and water concentrations,  
301 because the O<sub>2</sub>/N<sub>2</sub> ratio and water concentration affect the line width independently of  
302 pressure and O<sub>2</sub> concentration alone. To minimize systematic errors due to these broadening  
303 effects, we define a nominal  $y$ -parameter based on the measured amplitudes of the O<sub>2</sub> and  
304 water lines and the line broadening dependences shown in Figures 3 and 4. The measured  
305 ratio  $A_{O_2}/y$  is normalized by the nominal  $y$  to obtain a quantity that is ideally independent of  
306 pressure and water concentration, and this is the quantity that is multiplied by a calibration  
307 constant to give the reported O<sub>2</sub> fraction. In addition, a dry mole fraction is reported for O<sub>2</sub>,  
308 defined as the directly measured mole fraction corrected for water dilution.

309 The main goal in developing this instrument was to make high precision  
310 measurements of O<sub>2</sub> mole fraction, based on absorption by the dominant <sup>16</sup>O<sub>2</sub> isotopologue.



311 The absorption lines of the rarer isotopologues are also present nearby, so a mode of operation  
312 was included in which one laser is scanned over neighboring lines of  $^{16}\text{O}_2$  and  $^{16}\text{O}^{18}\text{O}$  and the  
313 ratio of amplitudes is used to derive an isotopic ratio, reported in the usual delta notation. In  
314 this case the operating pressure was reduced to 160 hPa to improve the resolution of the  
315 nearby lines. The lines measured were the Q3Q3 line of  $^{16}\text{O}_2$ , at  $7882.18670\text{ cm}^{-1}$ , and the  
316 Q9Q9 line of  $^{16}\text{O}^{18}\text{O}$ , at  $7882.050155\text{ cm}^{-1}$ . The measurement procedure is very much like  
317 that for the  $\text{O}_2$  fraction measurement, so it will not be described in detail, only the main  
318 differences will be noted. One is that in determining an isotopic ratio there is no advantage to  
319 be obtained from normalizing absorption amplitudes to line widths, instead we simply take  
320 the ratio of amplitudes to compute delta. Although the Q9Q9 line and its neighbor Q8Q8 are  
321 the strongest ones in this band, absorption by  $^{16}\text{O}^{18}\text{O}$  is still very weak, only about  $5 \times 10^{-9}\text{ cm}^{-1}$   
322 at the line center under the conditions we used. Consequently, the signal-to-noise that can be  
323 achieved with this analyzer is not adequate to determine both the amplitude and the width of  
324 the  $^{16}\text{O}^{18}\text{O}$  line with useful precision, so in the fitting step the y-parameter of the  $^{16}\text{O}^{18}\text{O}$  line  
325 is constrained to be a constant factor times the fitted y-parameter for the  $^{16}\text{O}_2$  line.  
326 Additionally, because of the weakness of the rare isotopologue absorption, the majority of  
327 ring-downs in each spectrum is devoted to measuring  $^{16}\text{O}^{18}\text{O}$  i.e. 232 ring-downs in each  
328 spectrum versus only 40 for  $^{16}\text{O}_2$ . This implies that the mole fraction measurement in the  
329 isotopic mode is much less precise than when the analyzer measures the Q13Q13 line alone.

### 330 **3. Results and Discussions**

#### 331 **3.1. Laboratory tests at Picarro, Santa Clara**

##### 332 3.1.1. Temperature and pressure sensitivity

333 One set of tests was done to determine how well the goal was met of minimizing the  
334 susceptibility of the concentration measurements to uncontrolled noise or drift of the sample



335 temperature and pressure. For these tests the analyzer sampled dry synthetic air from a tank  
336 and the temperature and pressure setpoints of the cavity were adjusted upward and downward  
337 from the nominal values, to obtain an estimate of the differential response. We express the  
338 sensitivity to experimental conditions in relative form, that is the derivative with respect to  
339 temperature or pressure divided by the signal under nominal conditions.

340 From these experiments, we determined a temperature sensitivity of  $-2.1 \times 10^{-4} \text{ K}^{-1}$  and  
341 a pressure sensitivity of  $+9.8 \times 10^{-6} \text{ hPa}^{-1}$ . The temperature sensitivity is somewhat larger than  
342 expected based on a calculation using Hitran data to estimate the temperature dependences of  
343 all the quantities that go into the measured absorption of the Q13Q13 line. The pressure  
344 sensitivity is strikingly small, indicating a good cancelation of the pressure dependence of  
345 absorption amplitude and line width. Both temperature and pressure sensitivities are small  
346 enough to have a negligible effect on short-term precision of measurements made with the  
347 stabilized ring-down cavity, though long-term drifts in the sensors are always a matter of  
348 concern.

### 349 3.1.2. Measurement precision and Drift

350 Measurement precision was evaluated by analyzing synthetic air containing nominal  
351 atmospheric concentrations of  $\text{CO}_2$  and  $\text{CH}_4$  from an aluminum Luxfer cylinder over a period  
352 of several days. The tank, oriented horizontally and thermally insulated (though not  
353 controlled), was connected directly to the instrument (S/N TADS2001) with a 2-stage  
354 regulator and stainless-steel tubing and reducing the flow with an additional orifice to about  
355 55 sccm. For the isotopic mode of operation, the precision of the measurement was also tested  
356 by making repeated measurements from a tank of clean, dry synthetic air.

357 Figure 8 shows the time series of the precision test data, displaying the reported  
358 oxygen concentration, the height of the oxygen absorption peak, the width of the oxygen



359 absorption peak and the ambient temperature. The residual drift of the analyzer, although  
360 small, is nevertheless significant given the stringent targets set forth by the WMO-GAW  
361 program. Possible sources of drift include: temperature drifts due to sensor drift or gradients;  
362 pressure errors due to sensor drift; optical artifacts such as parasitic reflections, higher order  
363 cavity mode excitation, and/or loss nonlinearity that can distort the reported oxygen spectrum.  
364 More work is required to identify and eliminate these small drifts.

365 The Allan standard deviation of the reported O<sub>2</sub> fraction is shown in Figure 9. The  
366 ordinate on this plot is the square root of the Allan variance of reported mole fraction, so 1  
367 ppm in these units corresponds to about 5 per meg in the ratio of O<sub>2</sub>/ N<sub>2</sub>. The precision of  
368 averaged measurements improves as  $\tau^{-1/2}$  for approximately 5000 s and reaches 1 ppm in less  
369 than 10 minutes and remains below 1 ppm for time scales on the order of about 1 hour.

370 Figure 10 shows the precision of  $\delta(^{18}\text{O})$  (uncalibrated) derived from the ratio of lines  
371 measured at 7882 cm<sup>-1</sup>. Because of the weak signal from the <sup>16</sup>O<sup>18</sup>O line, it is necessary to  
372 average for more than 20 seconds or more to achieve 1‰ precision on the isotopic ratio. As  
373 for the concentration measurement, averaging improves the measurement precision for times  
374 scale up to about 1 hour.

### 375 **3.2. Laboratory measurements at the University of Bern**

#### 376 3.2.1. Measurements of standard gases

377 The performance of the instrument was tested by analyzing eight standard gases with  
378 precisely known CO<sub>2</sub> and O<sub>2</sub> compositions (Table 1) using the CRDS analyzer and comparing  
379 it to parallel measurements with a paramagnetic oxygen sensor (PM1155 oxygen transducer,  
380 Servomex Ltd, UK) embedded to a commercially available Oxzilla fuel cell oxygen analyzer  
381 (OXZILLA II, Sable Systems International, USA) as well as with an isotope ratio mass  
382 spectrometer (IRMS, Finnigan Delta<sup>Plus</sup>XP). The design of the measurement set-up is shown





383 in Figure 11. Standard gases were directly connected to the pressure controlling unit, and a  
384 multi-port valve (V2) was used to select among the standard gases. The flow from each  
385 cylinder was adjusted to about  $120 \text{ ml min}^{-1}$  which was eventually directed to a selection  
386 valve (V1), allowing switching between ambient air and standard gases. Flow towards and out  
387 of the Oxzilla was controlled by the pressure controlling unit. The  $\text{O}_2$  mixing ratio of this  
388 incoming gas was first measured on the Paramagnetic  $\text{O}_2$  sensor and then directed towards a  
389 non-dispersive infrared analyzer (NDIR) (Li-7000, LICOR, USA) for measuring  $\text{CO}_2$  and  
390  $\text{H}_2\text{O}$ . The outflow from this analyzer ( $100 \text{ ml min}^{-1}$ ) returns to the pressure controlling unit  
391 and was eventually divided between the CRDS analyzer (which uses about  $75\text{-}80 \text{ ml min}^{-1}$ )  
392 and the IRMS ( $\sim 20 \text{ ml min}^{-1}$ ) via a Tee-junction. Each cylinder was measured for two hours  
393 in each system controlled by a Lab VIEW program.

394 In priori, we investigated the influence of this Tee-junction, which splits the gas flow  
395 between the CRDS and the IRMS, on the measured  $\text{O}_2$  values. Manning (2001) showed that  
396 the fractionation of  $\text{O}_2$  in the presence of a Tee-Junction is strongly dependent on the splitting  
397 ratios as well as temperature and pressure gradients. Hence, we measured and compared the  
398  $\text{O}_2$  mixing ratios of two standard gases (CA07045 and CA060943) in two cases: i) in the  
399 presence of a Tee-junction with different CRDS to IRMS splitting ratios and ii) without a  
400 Tee-junction so that all gas flow is directed towards the CRDS analyzer. The splitting ratios in  
401 these test experiments vary from 1:1 to 1:100, and reversed to change the major flow direction  
402 either to the CRDS or the IRMS. Note that the experimental condition in this manuscript is  
403 with a 4:1 splitting ratio (i.e.  $\sim 80 \text{ ml min}^{-1}$  towards the CRDS analyzer and  $\sim 20 \text{ ml min}^{-1}$   
404 towards the IRMS).

405 In the cases of the smaller splitting ratios (1:1, 1:4 and 4:1), which are relevant for the  
406 results presented in this study, only minor differences in the measured  $\text{O}_2$  mixing ratios were



407 observed when compared to case b (i.e. without a Tee-junction). For these two cylinders  
408 measured, the average differences in these cases were about 0.5 ppm, calculated as the mean  
409 of the differences in the raw O<sub>2</sub> measurements of the last 60 seconds. The negligible  
410 fractionation can indeed be the result of smaller splitting ratios while strong influence is  
411 usually expected in case of larger splitting ratios (Stephens et al., 2007). For higher splitting  
412 ratios, the result seems inconclusive without any dependence on the ratios due to the strong  
413 decline in the cylinder temperature (specifically at the pressure gauge) caused by higher flow  
414 to achieve the higher splitting ratios (as high as 1:100). Hence, these tests need to be  
415 conducted in a temperature controlled condition and the results could not be discussed in this  
416 manuscript.

417 Figure 12 shows the standard gas measurements for the seven cylinders with known  
418 CO<sub>2</sub> and O<sub>2</sub> mixing ratios (Table 1) using both the CRDS and the Paramagnetic analyzers.  
419 Standard eight, which has too high O<sub>2</sub>, is not shown in the figure as the figure is zoomed-in to  
420 better illustrate the change in O<sub>2</sub> for the remaining cylinders. While the first five cylinders  
421 contain O<sub>2</sub> and CO<sub>2</sub> fractions comparable to ambient air values, standards 6 & 8 had either  
422 very low and very high O<sub>2</sub>, respectively. In addition, standard 6 and 7 have very low and very  
423 high CO<sub>2</sub> mixing ratios. Note that due to its very high CO<sub>2</sub> content (~ 2700 ppm), standard 7  
424 was not measured on the IRMS and hence the O<sub>2</sub> mixing ratios are unknown. The measured  
425 mixing ratios for the six standard gases between the two systems are in very good agreement  
426 while cylinder 7 showed an opposing signal for the two analyzers compared to standard 6  
427 (Figure 12). While the Paramagnetic analyzer showed a higher O<sub>2</sub> mixing ratio, the values  
428 from the CRDS analyzer are lower in O<sub>2</sub>. This can be associated with the very high CO<sub>2</sub>  
429 mixing ratio in standard 7, which leads to a strong dilution effect in the CRDS analyzer as it  
430 does not include any correction function for dilution effect from CO<sub>2</sub>. However, such high



431 CO<sub>2</sub> mixing ratios may not be that important for most atmospheric research. Yet, it should be  
432 considered to include a parallel CO<sub>2</sub> mixing ratios measurement to the instrument as it will  
433 further improve the accuracy. This would be especially important for biological or  
434 physiological studies where a wide range of CO<sub>2</sub> and O<sub>2</sub> concentrations must be expected.

435 The measurement precision of the CRDS analyzer was calculated as the standard error  
436 of the mean i.e. the standard deviation (1- $\sigma$ ) of the last 1-minute raw measurements divided  
437 by the square root of the number of measurements ( $n = 60$ ), and for all these cylinders the  
438 values are usually between 0.5 ppm to 0.7 ppm. For parallel measurements of these cylinders  
439 using a Paramagnetic analyzer, we obtained a precision of about 1 ppm, calculated exactly the  
440 same way.

441 We also made a correlation plot to see which of the two instruments are in better  
442 agreement with the assigned values based on IRMS measurements for the individual  
443 cylinders. While similar correlation coefficients were observed for both analyzers, different  
444 slopes were calculated (Fig. A.1). This is due to the fact that the IRMS measures the O<sub>2</sub> to N<sub>2</sub>  
445 ratio ( $\delta(O_2/N_2)$ ) in per meg, while the CRDS and the Paramagnetic analyzers provide non-  
446 calibrated O<sub>2</sub> mixing ratios in units of ppm and per meg, respectively. If we exclude the two  
447 standard gases with the highest and lowest O<sub>2</sub> mixing ratios (standards 7 and 8) that are  
448 subjected to strong dilution effects, both the slope and the  $r^2$  values decrease from those  
449 shown in Figure A.1. But this decrease is larger in the case of the Paramagnetic  
450 measurements, implying a slightly better linearity of the CRDS analyzer.

#### 451 3.2.2. Measurements of ambient air

452 Ambient air measurements were conducted from the roof top of our laboratory at the  
453 University of Bern to evaluate the analyzer's performance under atmospheric variability.  
454 Ambient air was continuously aspirated from the inlet at the roof of the building at a flow rate



455 of  $\sim 250 \text{ ml min}^{-1}$  which is then dried using a cooling trap kept at  $-90 \text{ }^\circ\text{C}$  towards the  
456 switching valve (V1) and measured in similar way to the standard gases as explained above.  
457 The measurement values obtained here were compared with the parallel measurements by the  
458 Paramagnetic sensor to test the instruments stability and accuracy.

459         Figures 13 panels a & b show the 1-minute average ambient air measurements from the  
460 rooftop inlet by the Paramagnetic and the CRDS analyzers at the beginning of the testing  
461 period including standard gases measured every 12-hour. While the Paramagnetic analyzer  
462 seems to be stable, the CRDS analyzer showed a strong drift for an extended period. This can  
463 be due to unstable conditions in the CRDS measurement system as it started operating right  
464 after it was unpacked. Hence, we looked into its DAS temperature and pressure records,  
465 which were stable within the manufacturer's recommended range during this period. As the  
466 CRDS analyzer incorporates a water correction function, interference from this species should  
467 be well accounted. Even comparing the analyzer's parallel water measurements to water  
468 measurements by the NDIR system such a drift was not observed. It should be noted that the  
469 two internal standard gases which were less frequently measured (every 12 hours) during this  
470 period were also drifting in similar pattern. This implies that the drift is associated with the  
471 analyzer. Interestingly, we observed that the two cylinders follow exactly the same drift  
472 pattern that can be modeled using a polynomial function which can then be used to correct for  
473 the observed drift in the ambient air measurements. After applying a polynomial drift  
474 correction, we were able to fully account for the observed drift. However, the manufacturer  
475 decided to further investigate possible causes of this drift. After further improvements, we  
476 obtained the first commercial analyzer in September 2017 and repeated the above tests  
477 (Figure 13 c & d). No such drift was observed any more in the standard gases or in ambient air  
478 measurements.



## 479 3.2.3. Water correction test

480 Measurements of oxygen are reported as both wet ( $O_{2, \text{raw}}$ ) and dry ( $O_{2, \text{dry}}$ ) mole  
481 fractions by the CRDS analyzer as it also measures water vapor in parallel at its water  
482 absorption line ( $7817 \text{ cm}^{-1}$ ), and corrects for the dilution effect based on an inbuilt numerical  
483 function:

$$484 \quad O_{2, \text{dry}} = \frac{O_{2, \text{raw}}}{1 - f_{\text{H}_2\text{O}}} \quad (4)$$

485 where  $f_{\text{H}_2\text{O}}$  is the measured water mole fraction.

486 The efficiency of water correction by this function was assessed in two ways: i) by comparing  
487 the water vapor content in standard air measured by this analyzer with similar measurements  
488 by the NDIR analyzer and ii) by comparing the oxygen mixing ratios between non-dried  
489 ambient air measured and corrected for water dilution by the CRDS analyzer with dried air  
490 measured using a paramagnetic analyzer.

491 Figure 14 shows the water vapor content for standard gases measured continuously for  
492 two days by the CRDS and the NDIR analyzers. Note that the two data sets are manually  
493 fitted to each other as the measured water values by the NDIR analyzer are not calibrated.  
494 Based on these plots, the two analyzers are in very good agreement although there are small  
495 differences during very dry conditions (low water content).

496 The water correction test was conducted by measuring dried ambient air (Figure 15a)  
497 into both analyzers as well as allowing non-dried air to the CRDS analyzer only (Figure 15b)  
498 and comparing the difference in  $O_2$  measurements in both cases (Figures 15c & 15d). shows  
499 the water contents of dried ambient air measured in both analyzers while Figure 15b shows in  
500 case non-dried air is admitted to the picaro analyzer only (note that the CRDS uses its in-built  
501 water correction function). The measurements of the Paramagnetic analyzer were scaled to



502 ppm units by applying the correlation equation obtained from the six standard gas  
503 measurements of the two analyzers (Fig. A.1). Note that the CRDS measurements were  
504 corrected for the observed drift using the polynomial fit to the two standard gas measurements  
505 stated above.

506 In the first period of the measurement when both analyzers measured dried ambient  
507 air, the absolute differences between the 1-minute averages measured over two days by the  
508 two analyzers were mostly within 15 ppm and symmetrically distributed around zero.  
509 However, when wet air was admitted to the CRDS analyzer and the in-built water correction  
510 was applied, a stronger variability was observed in the calculated differences. This implies  
511 stronger short term variability in the CRDS analyzer measurement values (as nothing was  
512 changed for the Paramagnetic measurement system) when wet samples were analyzed. The  
513 more negative values in the differences can also be associated with overestimation of the O<sub>2</sub>  
514 mixing ratios by the CRDS originating from an overestimated water correction. However,  
515 detailed evaluation of the analyzer's water correction function is beyond the scope of this  
516 study.

### 517 3.3. Field Measurements

518 After a series of tests at University of Bern, we conducted multiple field measurements  
519 at the High Altitude Research Station Jungfrauoch and the Beromünster tall tower sites in  
520 Switzerland described below.

#### 521 3.3.1. Tests at the High Altitude Research station Jungfrauoch

522 The High Alpine research station Jungfrauoch is located on the northern ridge of the  
523 Swiss Alps (46° 33' N, 7° 59' E) at an elevation of 3580 m a.s.l. It is one of the global  
524 atmospheric watch (GAW) stations well-equipped for measurements of numerous species and  
525 aerosols. The site is above the planetary boundary layer most of the time due to its high



526 elevation (Henne et al., 2010; Zellweger et al., 2003). However, thermally uplifted air from  
527 the surrounding valleys during hot summer days or polluted air from the heavily industrialized  
528 northern Italy may reach at this site (Zellweger et al., 2003). The Division of Climate and  
529 Environmental Physics at the University of Bern has been monitoring CO<sub>2</sub> and O<sub>2</sub> mixing  
530 ratios at this site based on weekly flask sampling and continuous measurements since 2000  
531 and 2004, respectively. The CO<sub>2</sub> mixing ratio is measured using a commercial NDIR analyzer  
532 (S710 UNOR, SICK MAIHAK) while O<sub>2</sub> is measured using the Paramagnetic sensor  
533 (PM1155 oxygen transducer, Servomex Ltd, UK) and fuel cells (Max-250, Maxtec, USA)  
534 embedded within a home-built controlling unit. Similar to the comparison tests at the  
535 University of Bern, we have conducted parallel measurements between the CRDS analyzer  
536 and the paramagnetic cell at this high altitude site during 03 – 14 February 2017. The  
537 measurement of ambient air at the Jungfrauoch system is composed of sequential switching  
538 between a low span (LS) and high span (HS) calibration gases followed by a target gas (T)  
539 measurement (once a day) to evaluate the overall system performance and finally a working  
540 gas (WG) measurement before switching back to ambient air.

541 Figure 16 (top panel) shows the calibrated 1-minute averaged O<sub>2</sub> mixing ratios  
542 measured at this high altitude site in comparison with the Paramagnetic oxygen analyzer  
543 already available at the site. While a strong variability was observed during the measurement  
544 period of 10-days by both analyzers, a very good agreement was observed between them.

545 Figure 16 (bottom panel) shows the absolute difference of 1-minute averages in  
546 atmospheric O<sub>2</sub> measured at Jungfrauoch between the two analyzers which are mostly within  
547  $\pm 5$  ppm range (but sometimes going as high as  $\pm 10$  ppm) without an offset. However, for  
548 generally reported 10-minutes, half-hourly or hourly means these values correspond to  $< 1.5$   
549 ppm,  $< 1$  ppm and  $< 0.65$  ppm.



## 550 3.3.2. Tests at the Beromünster tall tower site

551 The Beromünster tower is located near the southern border of the Swiss Plateau, the  
552 comparatively flat part of Switzerland between the Alps in the south and the Jura mountains  
553 in the northwest (47° 11' 23" N, 8° 10' 32" E, 797 m a.s.l.), which is characterized by intense  
554 agriculture and rather high population density. A detailed description of the tower  
555 measurement system as well as a characterization of the site with respect to local  
556 meteorological conditions, seasonal and diurnal variations of greenhouse gases, and regional  
557 representativeness can be obtained from previous publications (Berhanu et al., 2016; Berhanu  
558 et al., 2017; Oney et al., 2015; Satar et al., 2016). The tower is 217.5 m tall with access to five  
559 sampling heights (12.5 m, 44.6 m, 71.5 m, 131.6 m, 212.5 m) for measuring CO, CO<sub>2</sub>, CH<sub>4</sub>  
560 and H<sub>2</sub>O using Cavity Ring Down Spectroscopy (Picarro Inc., G-2401). By sequentially  
561 switching from the highest to the lowest level, mixing ratios of these trace gases were  
562 recorded continuously for three minutes per height, but only the last 60 seconds were retained  
563 for data analysis. The calibration procedure for ambient air includes measurements of  
564 reference gases with high and low mixing ratios traceable to international standards (WMO-  
565 X2007 for CO<sub>2</sub> and WMO-X2004 for CO and CH<sub>4</sub>), as well as target gas and more frequent  
566 working gas determinations to ensure the quality of the measurement system. From two years  
567 of data a long-term reproducibility of 2.79 ppb, 0.05 ppm, and 0.29 ppb for CO, CO<sub>2</sub> and  
568 CH<sub>4</sub>, respectively was determined for this system (Berhanu et al., 2016).

569 Between 15.02.2017 and 02.03.2017, we have connected the new CRDS oxygen  
570 analyzer in series with the CO<sub>2</sub> analyzer (Picarro G-2401) and measured the O<sub>2</sub> mixing ratios  
571 at the corresponding heights. Similar to the CO<sub>2</sub> measurements, O<sub>2</sub> was also measured for  
572 three minutes at each height. During this period, we have evaluated the two features (isotopic  
573 mode and concentration mode) of the CRDS analyzer. In the isotopic mode, the CRDS





574 measures the  $\delta^{18}\text{O}$  values as well as the  $\text{O}_2$  concentration while in concentration mode only  
575 the latter was measured.

576         During the tests conducted at this tower site, we first evaluated the two operational  
577 modes (concentration vs isotopic modes) of the CRDS analyzer. Ambient air measurements  
578 on isotopic mode over a 4-days period showed a strong variability in the measured oxygen  
579 mixing ratios and it was not possible to distinguish the variability in the  $\text{O}_2$  mixing ratios  
580 among the five height levels. The calculated 1-minute standard error for ambient air  
581 measurements was as high as 10 ppm while a standard error of less than 1 ppm was  
582 determined from similar measurements in the concentration mode. Additionally, comparing  
583 the  $\text{O}_2$  values between the two modes, frequent short time variation in ambient air  $\text{O}_2$  (~ 200  
584 ppm) was observed in the isotope mode measurements while the variation in the concentration  
585 mode is significantly smaller (~ 30 ppm). This precision degradation is due to the weaker  $^{16}\text{O}$   
586 oxygen line used for the isotopic mode, and the fact that far more ring-downs are collected on  
587 the rare isotopologue in isotopic mode Hence, we have conducted the remaining test  
588 measurements in concentration mode.

589         As this tower has five sampling height levels, we first followed three minutes of  
590 switching per inlet level, which enables four measurements per hour at a given level.  
591 However, we noticed hardly any difference among the different levels due to strong short  
592 term variability in  $\text{O}_2$  mixing ratios between the consecutive heights. Hence, we switched to a  
593 longer sampling period of six-minutes per height. Figure 17 shows the diurnal  $\text{CO}_2$  and  $\text{O}_2$   
594 variations at the lowest (12 m) and highest (212.5 m) sampling heights of the tower. These  
595 two heights were selected simply to better illustrate the difference in the mixing ratios. The  
596  $\text{CO}_2$  mixing ratios on the top panel show higher values at the 12 m inlet than the highest level  
597 most of the day due to its closeness to sources except during the afternoon (11:00 - 17:00



598 UTC) when both levels show similar but decreasing CO<sub>2</sub> mixing ratios. This is due to  
599 presence of a well-mixed planetary boundary layer (PBL) (Satar et al., 2016). The lag in CO<sub>2</sub>  
600 peak between the two height levels by about two hours indicates the duration for uniform  
601 vertical mixing along the tower during winter 2017. The opposite variability patterns are also  
602 clearly visible in the O<sub>2</sub> mixing ratios shown in the lower panel with a clear distinction  
603 between the two height levels during early in the morning and in the evening while similar O<sub>2</sub>  
604 values were observed in the afternoon. These opposing profiles are expected as CO<sub>2</sub> and O<sub>2</sub>  
605 are linearly coupled with a mean oxidation ratio of  $-1.1 \pm 0.05$  (Severinghaus, 1995) for land-  
606 biospheric processes (photosynthesis and respiration) and  $-1.44 \pm 0.03$  for fossil fuel burning  
607 (Keeling, 1988b).

608 Table 2 shows the oxidation ratios derived as the slopes of the linear regression  
609 between CO<sub>2</sub> and O<sub>2</sub> mixing ratios at the different height levels measured on 25 February  
610 2017. Accordingly, height dependent slopes were observed with a slope of  $-0.98 \pm 0.06$  at the  
611 lowest level, close to the biological processes induced slope but slightly lower than its mean  
612 value. For the highest level, we calculated a slope of  $-1.60 \pm 0.07$  a value close to fossil fuel  
613 combustion oxidation ratio. Note that depending on fossil fuel type the oxidation ratio can  
614 range between  $-1.17$  and  $-1.95$  for coal and natural gas, respectively (Keeling, 1988b). While  
615 the slopes derived for the two other levels (44.6 m and 131.6 m) show similar values between  
616 the highest and lowest height levels, possibly from mixed sources, the middle level showed a  
617 slightly higher slope than these two levels but still in the large range between the lowest and  
618 highest inlet heights.

#### 619 3.4. Evaluation of the $\delta^{18}\text{O}$ measurements

620 To further evaluate the analyzer's performance in measuring stable oxygen isotopes,  
621 we conducted ambient air isotopic composition measurements as well as analyzed a standard



622 gas without CO<sub>2</sub> which has a known  $\delta^{18}\text{O}$  value. The choice of this CO<sub>2</sub>-free air standard gas  
623 is twofold: one it has a known  $\delta^{18}\text{O}$  value and second as it has no CO<sub>2</sub> possible interference  
624 from band overlap is avoided. For this test three 0.5 L glass flasks were preconditioned and  
625 filled with this standard gas to ambient pressure. These flasks were attached before or after  
626 the water trap (Fig. 11) and measured similar to ambient air measurements. These  
627 measurements were then compared with  $\delta(^{34}\text{O}/^{32}\text{O})$  values obtained by parallel measurements  
628 using our IRMS.

629 Figure 18 shows the  $\delta^{18}\text{O}$  values of ambient air from the roof top with three  
630 consecutive measurements of glass flasks filled with CO<sub>2</sub>-free air in-between followed by a  
631 fourth flask filled with breath air. An excellent agreement was observed for measurements  
632 from both instruments for the three flasks filled with a standard gas. However, the fourth flask  
633 with breath air showed a signal opposite to the measurements by the IRMS. As breath air  
634 contains large amount of water CO<sub>2</sub> in addition to O<sub>2</sub>, which can possibly interfere with the  
635 CRDS analyzer measurements, we have removed H<sub>2</sub>O and CO<sub>2</sub> by using a cryogenic trap (-  
636 130 °C) and in an additional experiment using Schütze reagent to remove both CO and CO<sub>2</sub>.  
637 However, we have not observed any improvement towards an agreement with the IRMS  
638 measurements. Therefore, any other gas component in the breath air must be relevant for the  
639 interference. Based on the absorption lines in the spectral range of the instrument ( $7878\text{ cm}^{-1}$ )  
640 retrieved from HITRAN database, we expect interference either from carbon monoxide (now  
641 excluded by the tests) or methane or VOCs including acetone, ethanol, methanol or isoprenes,  
642 all of which have been measured in breath air (Gao et al., 2017; Gottlieb et al., 2017; McKay  
643 et al., 1985; Ryter and Choi, 2013; Wolf et al., 2017). Further investigations have to shed light  
644 on these interferences in order to take corresponding action to surpass these shortcomings in  
645 the isotope analysis based on cavity ring-down spectroscopy.



646 **4. Conclusions**

647 We have thoroughly evaluated the performance of a new CRDS analyzer which  
648 measures O<sub>2</sub> mixing ratios and isotopic composition combining laboratory and field tests.  
649 Even if a drift in the analyzer was observed at the beginning of this study, which if it appears  
650 can be easily corrected by calibration, the recent analyzers built by the manufacturer did not  
651 show such instrumental drift. However, prior tests are recommended to see the analyzer's  
652 stability.

653 The T-split tests for the current measurement setup based on the measurements of two  
654 standard gases showed a difference within the measurement uncertainty. However, this effect  
655 may become significant while applying larger splitting ratios and we recommend conducting  
656 further experiments to accurately quantify this influence for larger splitting ratios.

657 We have observed a strong influence of dilution in the measured O<sub>2</sub> values during the  
658 presence of high CO<sub>2</sub> mixing ratios. Even if such an influence may not be critical for the  
659 present study, such an effect might be significant in other studies where higher CO<sub>2</sub> mixing  
660 ratios might be present and we recommend following a correction strategy based on parallel  
661 CO<sub>2</sub> measurements. This also applies for more accurate analysis.

662 The water correction applied by the instrument's in-built function seems to sufficiently  
663 correct for the water vapor influence. However, a larger variability of the difference was  
664 observed between the CRDS analyzer and the Paramagnetic cell when dried samples were  
665 used in both systems. This can possibly be due to an overcorrection by the water correction  
666 function of the CRDS analyzer when dried samples were used. This is particularly true for the  
667 very low water vapor range (< 100 ppm).

668 Based on the analysis of O<sub>2</sub> mixing ratios in the concentration and isotopic modes, we  
669 have observed about a significant decrease in precision (about ten-fold) in the latter



670 measurement mode. The measured  $\delta^{18}\text{O}$  values for the standard air by the CRDS analyzer are  
671 in excellent agreement with the IRMS values. However, such measurements for a breath air  
672 showed a contrasting signal, possibly due to interference from other gases as breath air  
673 contains  $\text{CO}_2$ ,  $\text{CH}_4$  and  $\text{CO}$  in addition to oxygen. Hence, we recommend further investigation  
674 on such possible contaminants and how to possibly remove them while conducting ambient  
675 air measurements.

#### 676 **Acknowledgement**

677 We would like to thank ICOS-RI and the Swiss National Science Foundation (SNF) for  
678 funding ICOS-CH (20FI21\_148994, 20FI21\_148992). We are also grateful to the  
679 International Foundation High Alpine Research Stations Jungfrauoch and Gornergrat. The  
680 measurement system at the Beromünster tower was built and maintained by the CarboCount-  
681 CH (CRSII2\_136273) and IsoCEP (200020\_172550) projects both funded by SNF.

682

683

684

685

686

687

688

689

690

691

692

693



694 List of Tables

695 Table 1. Assigned mixing ratios of standard gases used in this study and their corresponding  
 696 values measured by the NDIR, CRDS and IRMS at the University of Bern. <sup>1</sup>The assigned  
 697 values are based on measurements from different institutions (University of Bern (UB),  
 698 Scripps or NOAA, see column cylinder name). <sup>2</sup>Measurements are on the Bern scale for CO<sub>2</sub>  
 699 and O<sub>2</sub>. The Bern scale is shifted by +550 per meg. <sup>3</sup>Values on the Scripps scale.

700

Cylinder name	Assigned CO <sub>2</sub> (ppm) <sup>1</sup>	Assigned O <sub>2</sub> (per meg) <sup>1</sup>	CO <sub>2</sub> -IRMS (ppm) <sup>2</sup>	CO <sub>2</sub> -NDIR (ppm) <sup>2</sup>	O <sub>2</sub> -IRMS (per meg) <sup>2</sup>	O <sub>2</sub> -Paramagnetic (per meg) <sup>2</sup>	O <sub>2</sub> -CRDS (per meg) <sup>2</sup>
ST-1 LUX3576-UB	427.47	-1026	427.47	427.59	-1026	-1070	-1057
ST-2 LK922131-UB	368.09	599	368.09	367.82	599	560	590
ST-3 CA07045-Scripps	382.303	-271.6	382.50	381.99	278 (-272.2) <sup>3</sup>	302	281
ST-4 CA07043-Scripps	390.528	-476.4	390.69	390.15	71 (-479.5) <sup>3</sup>	66	63
ST-5 CA07047-Scripps	374.480	-807.7	374.70	374.17	-253 (-803.3) <sup>3</sup>	-212	-233
ST-6 CA04556-NOAA	192.44	-3410	191.21	191.64	-3410	-2905	-3013
ST-7 CA06943-	2699.45	-		2612.80	-	-2691	-3369



NOAA							
ST-8 LK76852- UB	411.49	37794	411.49	406.25	37794	34513	36017

701

702

703 Table 2. The CO<sub>2</sub> and O<sub>2</sub> correlation coefficients at the different height levels derived using  
 704 the least square fit and the correlation coefficients ( $r^2$ ). Uncertainties are calculated as  
 705 standard error of the slope.

Height	Oxidation Ratios (O <sub>2</sub> :CO <sub>2</sub> )
12.5 m	-0.98 ± 0.06 (0.48)
44.6 m	-1.29 ± 0.07 (0.50)
71.5 m	-1.49 ± 0.08 (0.47)
131.6 m	-1.23 ± 0.05 (0.55)
212.5 m	-1.60 ± 0.07 (0.61)

706

707

708

709

710

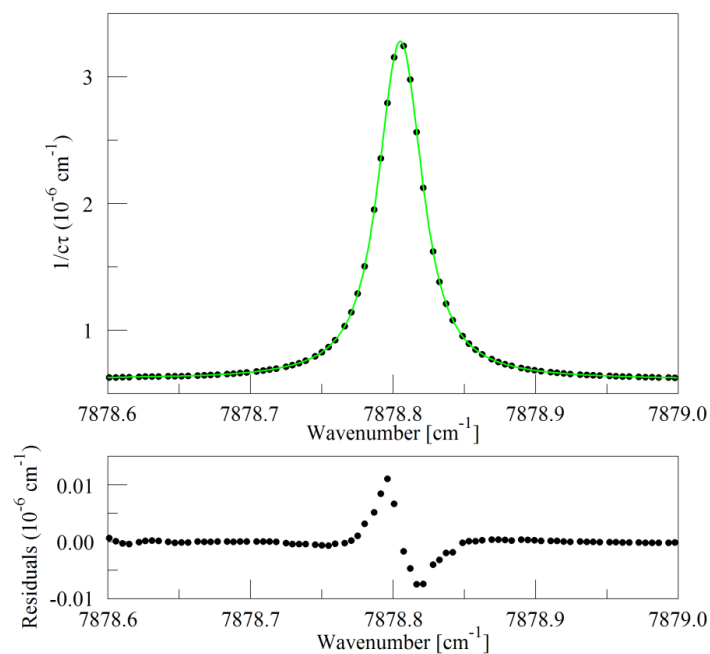
711

712

713



714 List of Figures



715

716 Figure 1. The Q13Q13 line of O<sub>2</sub> measured in a sample of synthetic air at a sample  
717 temperature and pressure of 45° C and 333 hPa, respectively.

718

719

720

721

722

723

724

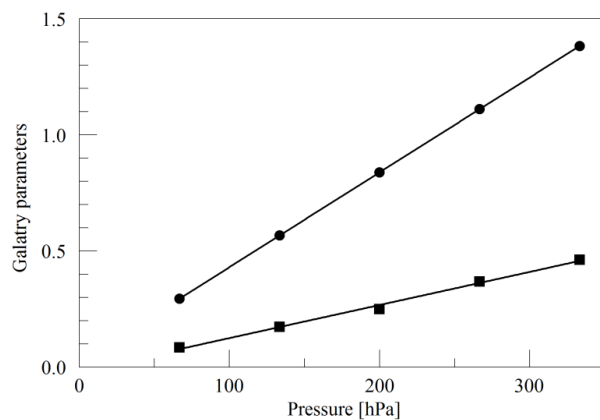
725

726



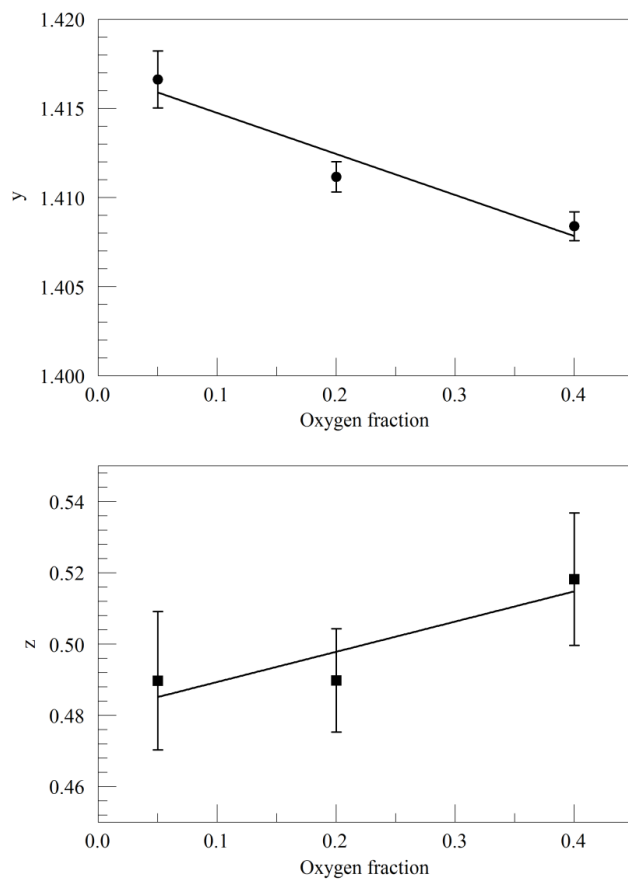


727



728

729 Figure 2. Best-fit values for the Galatry parameters of the Q13Q13 line of O<sub>2</sub>, as a function of  
730 pressure. The line broadening parameter  $y$  is represented by circles and the line narrowing  
731 parameter  $z$  by squares. The solid lines are linear fits to the measurements. The best-fit offset  
732 and slope are 0.0227 and 0.004082 hPa<sup>-1</sup> for  $y$ , and -0.0169 and 0.001424 hPa<sup>-1</sup> for  $z$ .

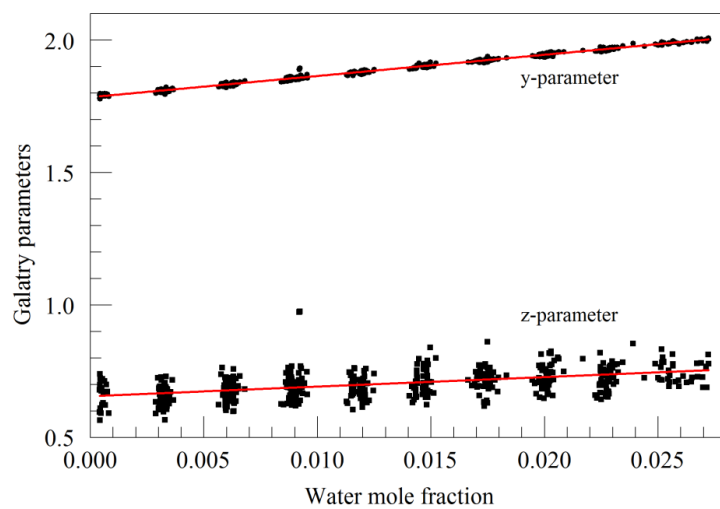


733

734 Figure 3. Galatry parameters of the Q13Q13 line of O<sub>2</sub> at 340 hPa and 45° C as a function of

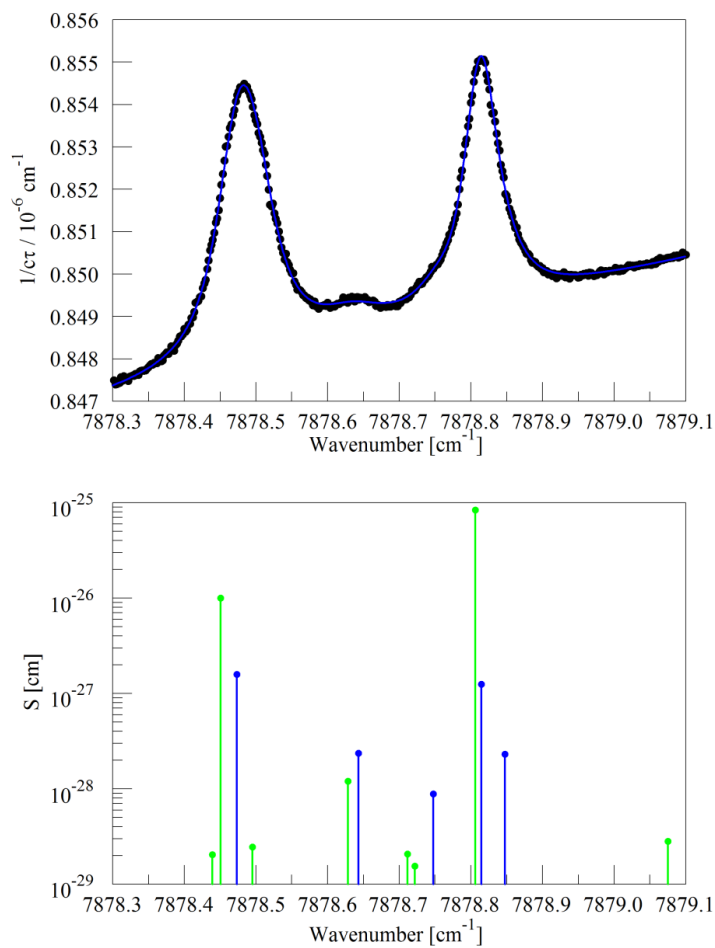
735 O<sub>2</sub> mole fraction in binary O<sub>2</sub> - N<sub>2</sub> mixtures.

736 The linear fits to the data are  $y = 1.417 - 0.023 \times f_{O_2}$  and  $z = 0.481 + 0.085 \times f_{O_2}$ .



737

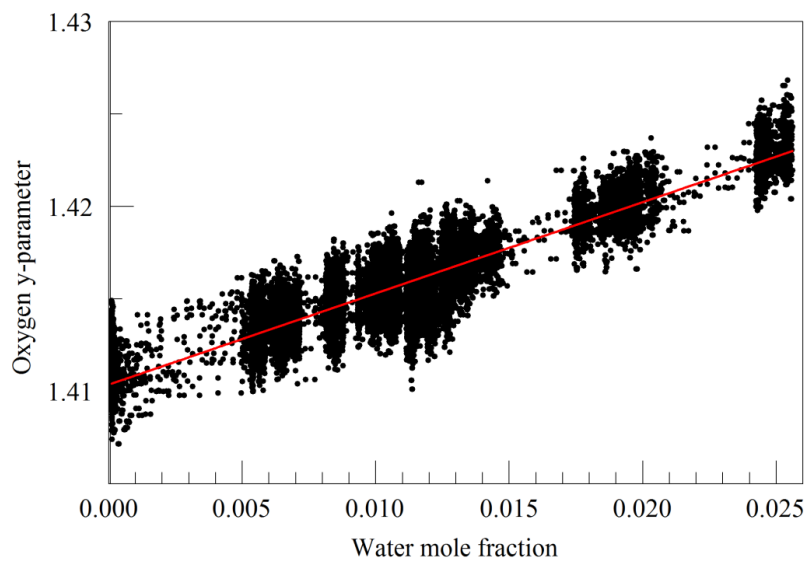
738 Figure 4. Galatry parameters of the  $7816.75210 \text{ cm}^{-1}$  water line in air at 340 hPa and  $45^\circ \text{ C}$  as  
739 a function of water mole fraction. Black points are from measurements and red lines are  
740 linear fits:  $y = 1.7846 + 8.01 \times f_{\text{H}_2\text{O}}$  and  $z = 0.656 + 3.60 \times f_{\text{H}_2\text{O}}$ .



741

742 Figure 5. Upper panel: spectrum of water in nitrogen (points) and fit to Voigt model (blue

743 curve). Lower panel: Oxygen (green) and water (blue) lines in the Hitran database.



744

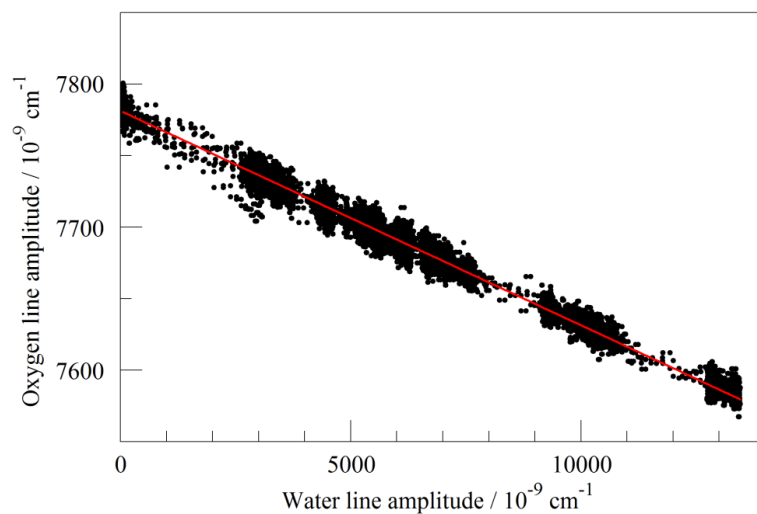
745 Figure 6. Galatry collisional broadening parameter of the oxygen Q13Q13 line at 340 hPa  
746 and 45° C versus water mole fraction. Black points are from measurements and the red line is  
747 a linear fit:  $y = 1.4109 + 0.467 f_{\text{H}_2\text{O}}$ .

748

749

750

751



752

753

754 Figure 7. Measured absorption line amplitudes for oxygen and water vapor for water vapor  
755 mixing ratios ranging from nearly 0 to 0.025. Black points are from measurements and the  
756 red line is a linear fit: with intercept  $7.78001 \times 10^{-6} \text{ cm}^{-1}$  and slope  $-0.014807$ .

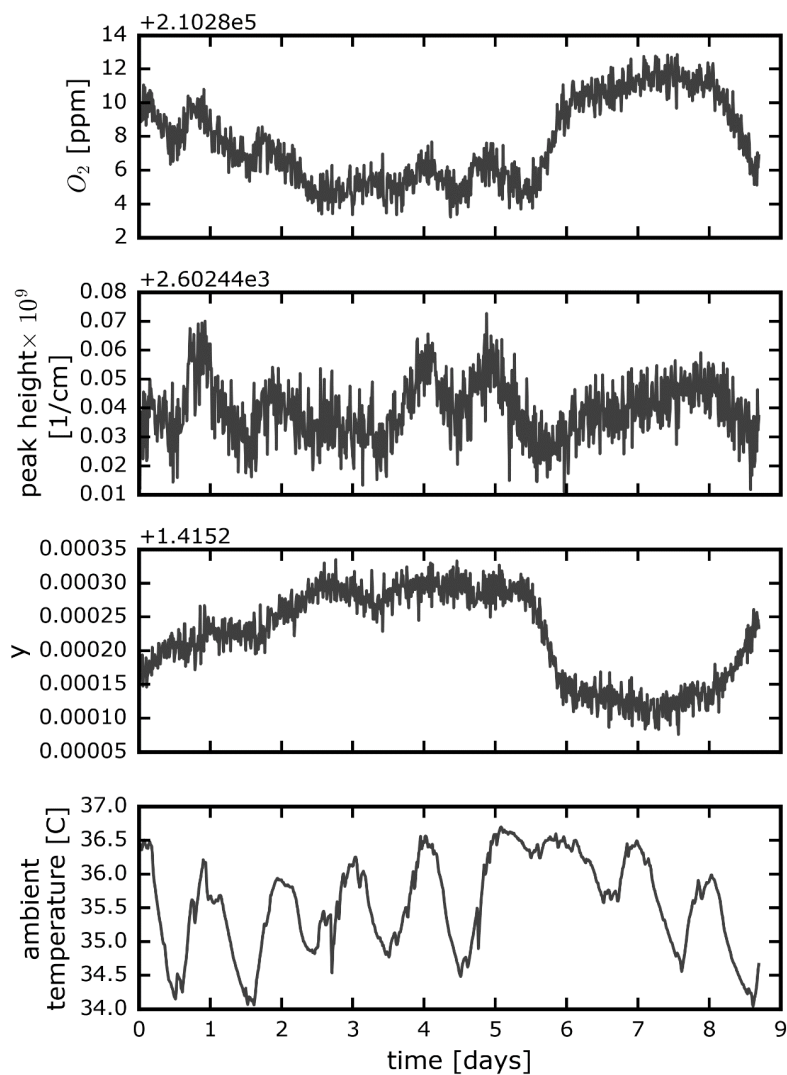
757

758

759

760

761



762

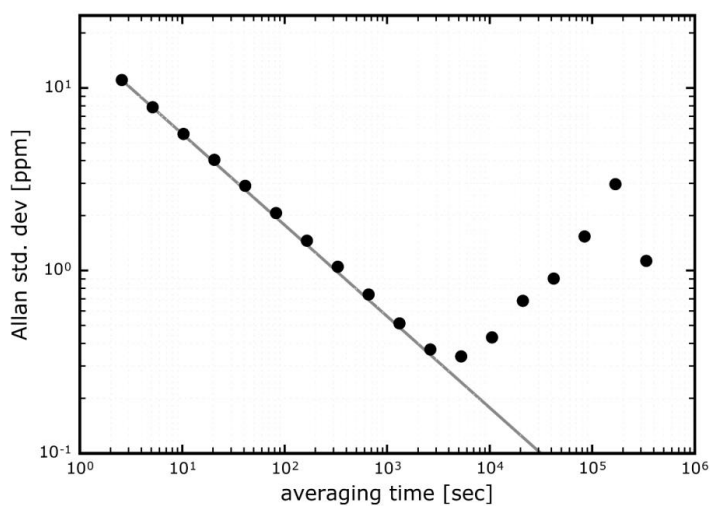
763 Figure 8. Time series from a measurement of a single tank over about a week. The four panels

764 shown the water-corrected oxygen concentration, the absorption peak loss minus the baseline

765 loss, the measured Lorentzian broadening factor, and the ambient temperature (measured in

766 the instrument housing), respectively. A windowed average of 300 seconds was applied to all

767 four data sets.



768

769 Figure 9. Precision of O<sub>2</sub> mole fraction measured from a tank of synthetic air. Filled circles

770 are measurements and the line shows the ideal  $\tau^{-1/2}$  dependence.

771

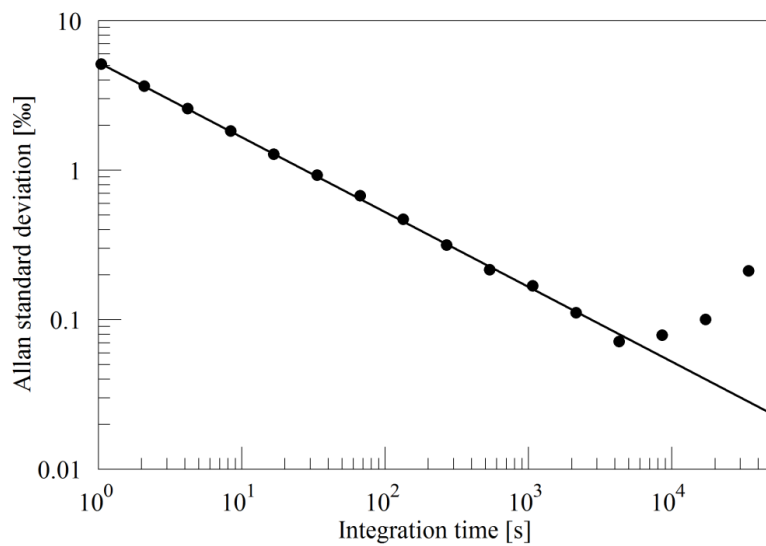
772

773

774

775





776

777 Figure 10. Precision of  $\delta(^{18}\text{O})$  measured from a tank of synthetic air. Filled circles are  
778 measurements and the line shows the ideal  $\tau^{-1/2}$  dependence.

779

780

781

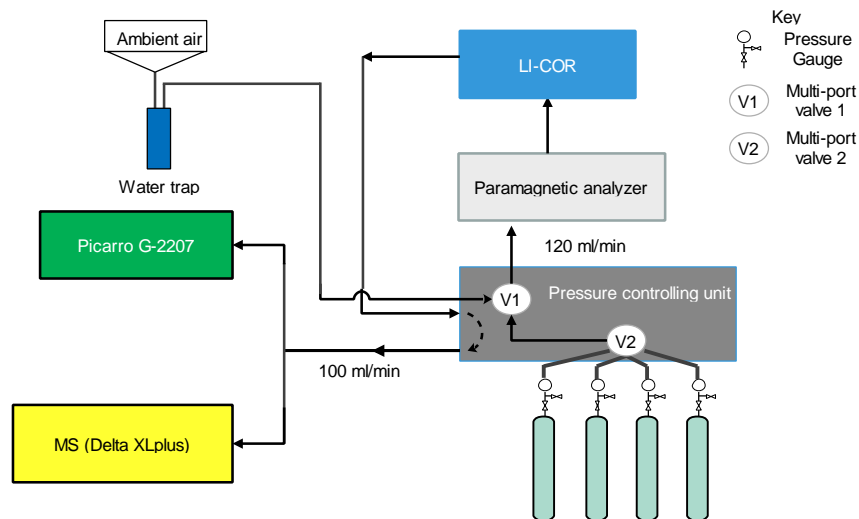
782

783

784

785

786



787

788 Figure 11. Schematics of the measurement system used to compare the Picarro analyzer with

789 the Mass Spectrometer at Bern.

790

791

792

793

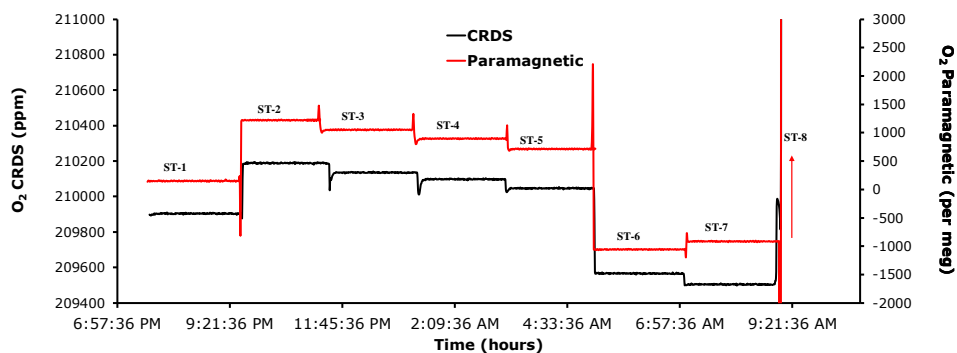
794

795

796

797

798



799

800 Figure 12. Comparison of oxygen mixing ratios for the seven standard gases measured using  
801 the CRDS analyzer (black) and the Paramagnetic sensors (red).

802

803

804

805

806

807

808

809

810

811

812

813

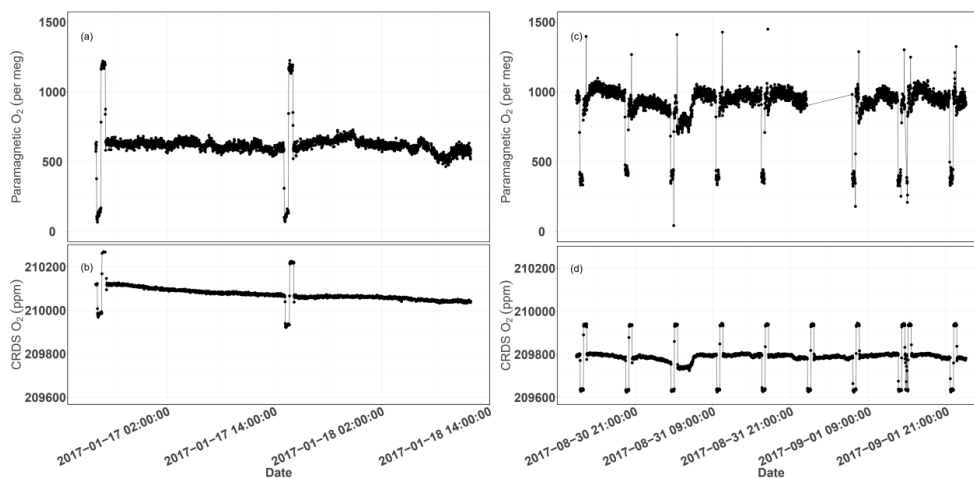
814

815

816



817



818

819 Figure 13. Parallel ambient air measurements by the Paramagnetic and CRDS analyzers at the  
820 beginning of the testing period (Panels a & b, January 2017) and the second phase of testing  
821 (Panels c & d, September 2017). The spikes are measurements from the two standard gases  
822 bracketing the ambient air values.

823

824

825

826

827

828

829

830

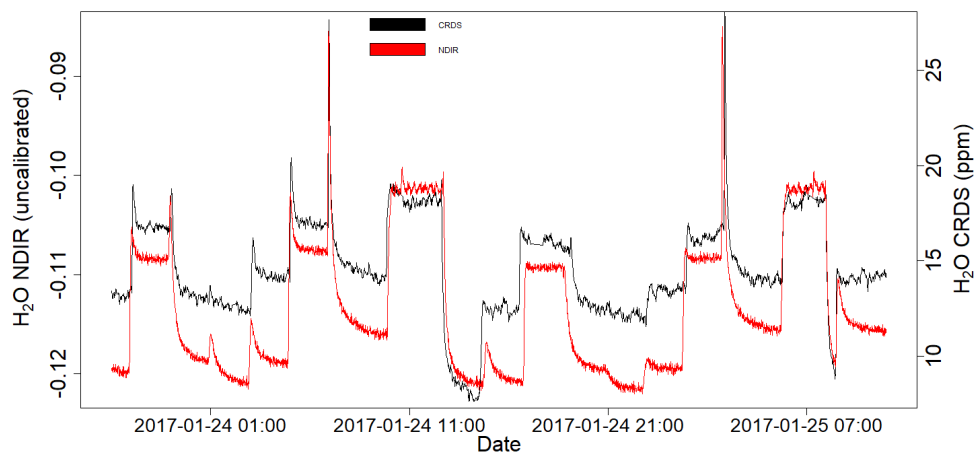
831

832

833



834



835

836 Figure 14. Parallel water vapor measurements for a dried ambient air by both the NDIR and

837 CRDS analyzers. Note that the water values from the NDIR analyzer are not calibrated.

838

839

840

841

842

843

844

845

846

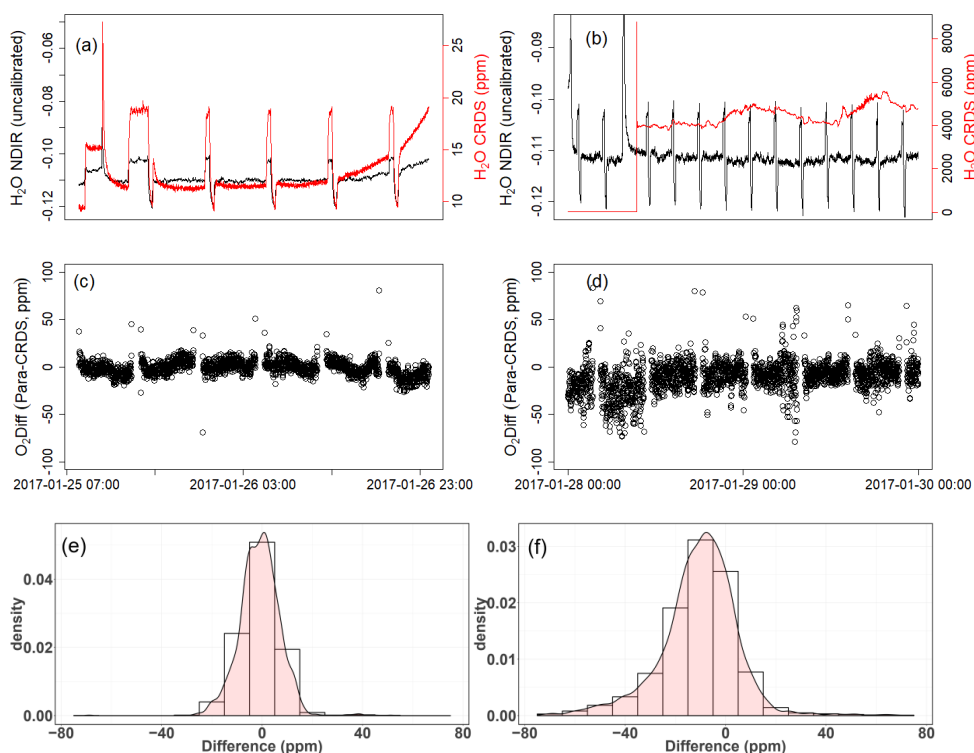
847

848

849



850



851 Figure 15. Results of water correction tests. Water measurements of the NDIR (left scale) for  
852 dry conditions (a,b) and the CRDS analyzer (right scale) for dry (a) and wet (b) conditions.  
853 The difference in oxygen measurements between the Paramagnetic and the CRDS instrument  
854 using the built-in water correction for the CRDS values under dry (c) and wet (d) conditions.  
855 Panels (e) and (f) show the population density functions.

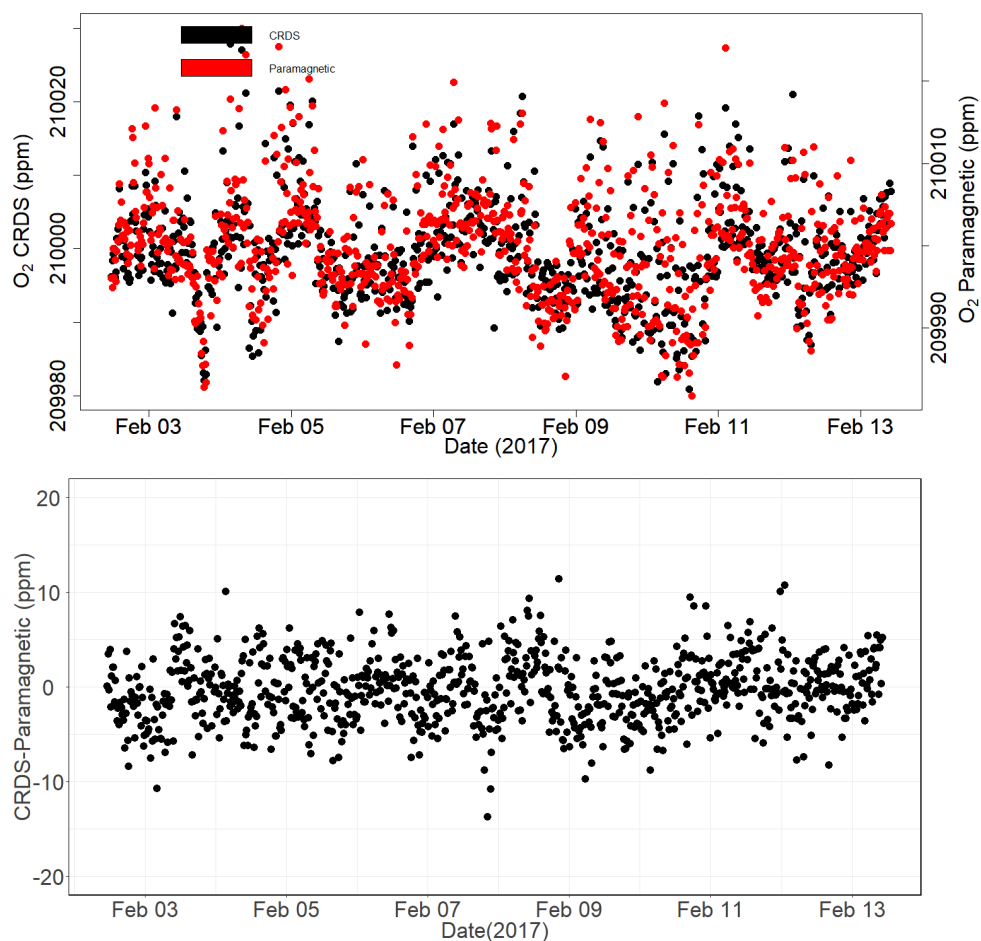
856

857

858

859

860



861

862

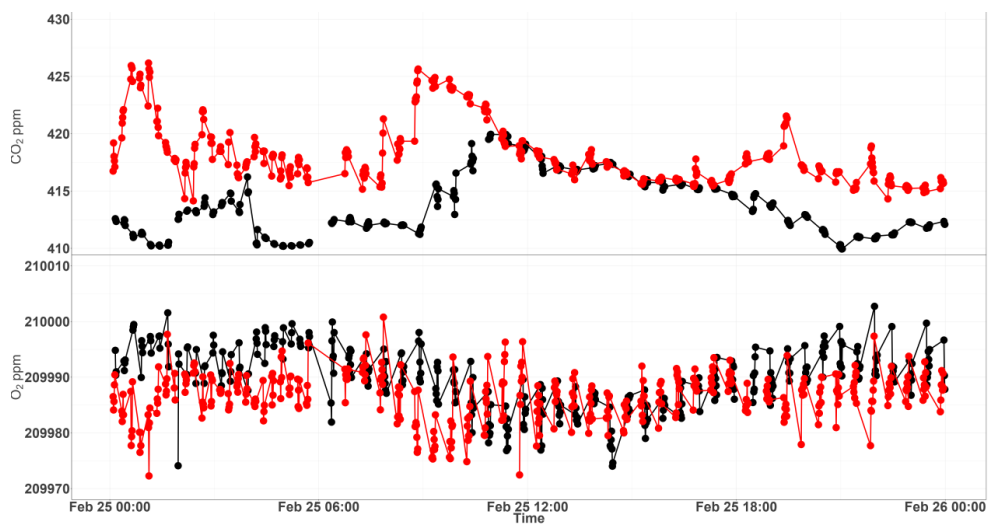
863 Figure 16. Calibrated ambient air oxygen measurements (1-minute average) at the  
864 Jungfraujoch site using the CRDS and Paramagnetic analyzers both in ppm units (a) and the  
865 absolute difference between the two measurements in ppm (b) by matching time stamps.

866

867

868

869



870

871 Figure 17. Diurnal variations of CO<sub>2</sub> (top) and O<sub>2</sub> (bottom) measurements from the 12 m (red)  
872 and the 212.5 m (black) height levels at Beromünster tower.

873

874

875

876

877

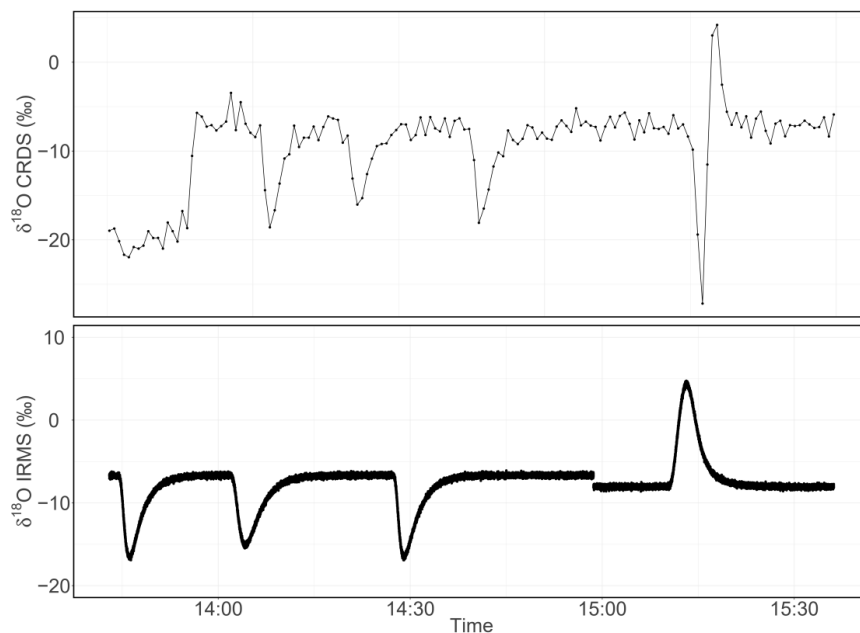
878

879

880

881





882

883 Figure 18. Consecutive  $\delta^{18}\text{O}$  measurements of a standard gas ( $\text{CO}_2$ -free air) filled into three

884 flasks followed by measurement of breath air using the CRDS analyzer (top) and IRMS

885 (bottom). These measurements were carried out in the middle of ambient air measurements.

886

887

888

889

890

891

892

893

894

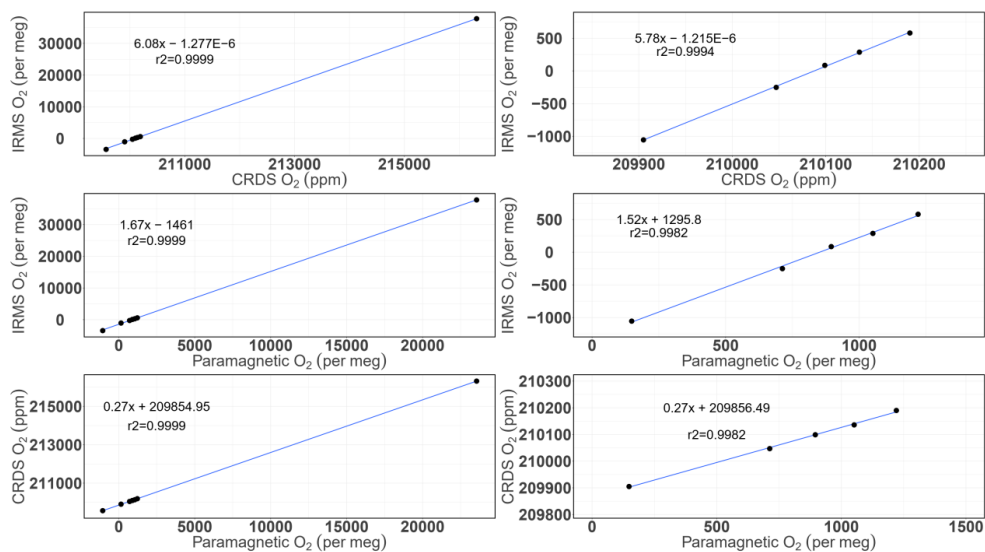
895



896 **Appendix A.**

897 **Additional plots**

898



899

900 Figure A.1. Correlations between the O<sub>2</sub> mixing ratios measured by the CRDS and  
901 Paramagnetic analyzers with the mass spectrometric measurements (uncalibrated values). The  
902 left panels are for all the cylinders measured (standards 1 to 8) while the right ones are after  
903 zooming only to standards 1-5.

904

905

906

907

908

909

910



911 **References**

- 912 Battle, M., Bender, M. L., Tans, P. P., White, J. W. C., Ellis, J. T., Conway, T., and Francey, R. J.: Global  
913 carbon sinks and their variability inferred from atmospheric O-2 and delta C-13, *Science*, 287, 2467-  
914 2470, 2000.
- 915 Bender, M. L., Tans, P. P., Ellis, J. T., Orchardo, J., and Habfast, K.: A High-Precision Isotope Ratio  
916 Mass-Spectrometry Method for Measuring the O-2 N-2 Ratio of Air, *Geochim Cosmochim Ac*, 58,  
917 4751-4758, 1994.
- 918 Berhanu, T. A., Satar, E., Schanda, R., Nyfeler, P., Moret, H., Brunner, D., Oney, B., and Leuenberger,  
919 M.: Measurements of greenhouse gases at Beromünster tall tower station in Switzerland, *Atmos.*  
920 *Meas. Tech.* , 9, 2016.
- 921 Berhanu, T. A., Szidat, S., Brunner, D., Satar, E., Schanda, R., Nyfeler, P., Battaglia, M., Steinbacher,  
922 M., Hammer, S., and Leuenberger, M.: Estimation of the fossil-fuel component in atmospheric CO2  
923 based on radiocarbon measurements at the Beromünster tall tower, Switzerland, *Atmos. Chem.*  
924 *Phys. Discuss.*, 2017, 1-33, 2017.
- 925 Crosson, E. R. J. A. P. B.: A cavity ring-down analyzer for measuring atmospheric levels of methane,  
926 carbon dioxide, and water vapor, 92, 403-408, 2008.
- 927 Filges, A., Gerbig, C., Rella, C. W., Hoffnagle, J., Smit, H., KrÄmmer, M., Spelten, N., Rolf, C., BozÄki, Z.,  
928 Buchholz, B., and Ebert, V.: Evaluation of the IAGOS-Core GHG Package H2O measurements during  
929 the DENCHAR airborne inter-comparison campaign in 2011, *Atmos. Meas. Tech. Discuss.*, doi:  
930 10.5194/amt-2018-36, 2018. 2018.
- 931 Fleisher, A. J., Hodges, J., and Sironneau, V.: Collision-dependent line areas in the  $\nu_1$  band  
932 of molecular oxygen, 2015.
- 933 Gao, F., Zhang, X., Zhang, X., Wang, M., and Wang, P.: Virtual electronic nose with diagnosis model  
934 for the detection of hydrogen and methane in breath from gastrointestinal bacteria, 28-31 May 2017  
935 2017, 1-3.



936 Gordon, E., Rothman, S., Hill, C., Kochanov, V., Tan, Y., Bernath, P., Birk, M., Boudon, V., Campargue,  
937 A., Chance, K., Drouin, J., Flaud, J., Gamache, R. R., Hodges, J., Jacquemart, D., Perevalov, I., Perrin, A.,  
938 Shine, P., Smith, M., Tennyson, J., Toon, G., Tran, H., Tyuterev, G., Barbe, A., Császár, G., Devi, M.,  
939 Furtenbacher, T., Harrison, J., Hartmann, J., Jolly, A., Johnson, J., Karman, T., Kleiner, I., Kyuberis, A.  
940 A., Loos, J., Lyulin, M., Massie, S., Mikhailenko, S., Moazzen-Ahmadi, N., Muller, S., Naumenko, O. V.,  
941 Nikitin, A. V., Polyansky, O. L., Rey, M., Rotger, M., Sharpe, S., Sung, K., Starikova, E., Tashkun, S.,  
942 Auwera, J., Wagner, G., Wilzewski, J., Wcisło, P., Yu, S., and Zak, E. J.: The HITRAN2016 molecular  
943 spectroscopic database, 203, 3 - 69, 2017.

944 Goto, D., Morimoto, S., Ishidoya, S., Aoki, S., and Nakazawa, T.: Terrestrial biospheric and oceanic  
945 CO<sub>2</sub> uptake estimated from long-term measurements of atmospheric CO<sub>2</sub> mole fraction,  $\delta^{13}\text{C}$  and  
946  $\delta(\text{O}_2/\text{N}_2)$  at Ny-Ålesund, Svalbard, Journal of Geophysical Research: Biogeosciences, doi:  
947 10.1002/2017JG003845, 2017. n/a-n/a, 2017.

948 Gottlieb, K., Le, C. X., Wachter, V., Sliman, J., Cruz, C., Porter, T., and Carter, S.: Selection of a cut-off  
949 for high- and low-methane producers using a spot-methane breath test: results from a large north  
950 American dataset of hydrogen, methane and carbon dioxide measurements in breath, Gastroenterol  
951 Rep, 5, 193-199, 2017.

952 Hartmann, J.-M., Boulet, C., and Robert, D.: Collisional Effects on Molecular Spectra, Elsevier Science,  
953 2008.

954 Henne, S., Brunner, D., Folini, D., Solberg, S., Klausen, J., and Buchmann, B.: Assessment of  
955 parameters describing representativeness of air quality in-situ measurement sites, Atmos. Chem.  
956 Phys., 10, 3561-3581, 2010.

957 Hodges, J. T., Layer, H. P., Miller, W. W., and Scace, G. E.: Frequency-stabilized single-mode cavity  
958 ring-down apparatus for high-resolution absorption spectroscopy, 75, 849-863, 2004.

959 Keeling, R. F.: Development of an Interferometric Oxygen Analyzer for Precise Measurement of the  
960 Atmospheric O<sub>2</sub> Mole Fraction, UMI, 1988a.



961 Keeling, R. F.: Measuring correlations between atmospheric oxygen and carbon dioxide mole  
962 fractions: A preliminary study in urban air, *J Atmos Chem*, 7, 153-176, 1988b.

963 Keeling, R. F. and Manning, A. C.: 5.15 - Studies of Recent Changes in Atmospheric O<sub>2</sub> Content A2 -  
964 Holland, Heinrich D. In: *Treatise on Geochemistry (Second Edition)*, Turekian, K. K. (Ed.), Elsevier,  
965 Oxford, 2014.

966 Keeling, R. F. and Shertz, S. R.: Seasonal and Interannual Variations in Atmospheric Oxygen and  
967 Implications for the Global Carbon-Cycle, *Nature*, 358, 723-727, 1992.

968 Keeling, R. F., Stephens, B. B., Najjar, R. G., Doney, S. C., Archer, D., and Heimann, M.: Seasonal  
969 variations in the atmospheric O<sub>2</sub>/N<sub>2</sub> ratio in relation to the kinetics of air-sea gas exchange, *Global*  
970 *Biogeochem Cy*, 12, 141-163, 1998.

971 Lamouroux, J., Sironneau, V., Hodges, J. T., and Hartmann, J. M.: Isolated line shapes of molecular  
972 oxygen: Requantized classical molecular dynamics calculations versus measurements, *Physical*  
973 *Review A*, 89, 042504, 2014.

974 Le Quéré, C., Andrew, R. M., Friedlingstein, P., Sitch, S., Pongratz, J., Manning, A. C., Korsbakken, J. I.,  
975 Peters, G. P., Canadell, J. G., Jackson, R. B., Boden, T. A., Tans, P. P., Andrews, O. D., Arora, V. K.,  
976 Bakker, D. C. E., Barbero, L., Becker, M., Betts, R. A., Bopp, L., Chevallier, F., Chini, L. P., Ciais, P.,  
977 Cosca, C. E., Cross, J., Currie, K., Gasser, T., Harris, I., Hauck, J., Haverd, V., Houghton, R. A., Hunt, C.  
978 W., Hurtt, G., Ilyina, T., Jain, A. K., Kato, E., Kautz, M., Keeling, R. F., Klein Goldewijk, K., Körtzinger, A.,  
979 Landschützer, P., Lefèvre, N., Lenton, A., Lienert, S., Lima, I., Lombardozzi, D., Metzl, N., Millero, F.,  
980 Monteiro, P. M. S., Munro, D. R., Nabel, J. E. M. S., Nakaoka, S. I., Nojiri, Y., Padín, X. A., Pregon, A.,  
981 Pfeil, B., Pierrot, D., Poulter, B., Rehder, G., Reimer, J., Rödenbeck, C., Schwinger, J., Séférian, R.,  
982 Skjelvan, I., Stocker, B. D., Tian, H., Tilbrook, B., van der Laan-Luijkx, I. T., van der Werf, G. R., van  
983 Heuven, S., Viovy, N., Vuichard, N., Walker, A. P., Watson, A. J., Wiltshire, A. J., Zaehle, S., and Zhu,  
984 D.: Global Carbon Budget 2017, *Earth Syst. Sci. Data Discuss.*, 2017, 1-79, 2017.



985 Manning, A.: Temporal variability of atmospheric oxygen from both continuous and measurements  
986 and a flask sampling network: tools for studying the global carbon cycle, Ph.D. Ph.D., University of  
987 California, San Diego, San Diego, California, USA, 2001.

988 Manning, A. C. and Keeling, R. F.: Global oceanic and land biotic carbon sinks from the Scripps  
989 atmospheric oxygen flask sampling network, *Tellus B*, 58, 95-116, 2006.

990 Manning, A. C., Keeling, R. F., and Severinghaus, J. P.: Precise atmospheric oxygen measurements  
991 with a paramagnetic oxygen analyzer, *Global Biogeochem Cy*, 13, 1107-1115, 1999.

992 Marrero, T. R. and Mason, E. A.: Gaseous Diffusion Coefficients, *Journal of Physical and Chemical*  
993 *Reference Data* 1, 3, 1972.

994 Martin, N. A., Ferracci, V., Cassidy, N., and Hoffnagle, J. A. J. A. P. B.: The application of a cavity ring-  
995 down spectrometer to measurements of ambient ammonia using traceable primary standard gas  
996 mixtures, 122, 219, 2016.

997 McKay, L. F., Eastwood, M. A., and Brydon, W. G.: Methane Excretion in Man - a Study of Breath,  
998 Flatus, and Feces, *Gut*, 26, 69-74, 1985.

999 Nevison, C. D., Keeling, R. F., Kahru, M., Manizza, M., Mitchell, B. G., and Cassar, N.: Estimating net  
1000 community production in the Southern Ocean based on atmospheric potential oxygen and satellite  
1001 ocean color data, *Global Biogeochem Cy*, 26, 2012.

1002 Oney, B., Henne, S., Gruber, N., Leuenberger, M., Bamberger, I., Eugster, W., and Brunner, D.: The  
1003 CarboCount CH sites: characterization of a dense greenhouse gas observation network, *Atmos.*  
1004 *Chem. Phys.*, 15, 11147-11164, 2015.

1005 Press, W. H., Teukolsky, S. A., Vetterling, W. T., and Flannery, B. P.: Numerical Recipes 3rd Edition:  
1006 The Art of Scientific Computing, Cambridge Printing Press, Cambridge, England, 1986.

1007 Press, W. H., Teukolsky, S. A., Vetterling, W. T., and Flannery, B. P.: Numerical recipes in C: the art of  
1008 scientific computing, Cambridge University Press, London, 1992.



- 1009 Rothman, L. S., Gordon, I. E., Babikov, Y., Barbe, A., Chris Benner, D., Bernath, P. F., Birk, M.,  
1010 Bizzocchi, L., Boudon, V., Brown, L. R., Campargue, A., Chance, K., Cohen, E. A., Coudert, L. H., Devi, V.  
1011 M., Drouin, B. J., Fayt, A., Flaud, J. M., Gamache, R. R., Harrison, J. J., Hartmann, J. M., Hill, C., Hodges,  
1012 J. T., Jacquemart, D., Jolly, A., Lamouroux, J., Le Roy, R. J., Li, G., Long, D. A., Lyulin, O. M., Mackie, C.  
1013 J., Massie, S. T., Mikhailenko, S., Müller, H. S. P., Naumenko, O. V., Nikitin, A. V., Orphal, J., Perevalov,  
1014 V., Perrin, A., Polovtseva, E. R., Richard, C., Smith, M. A. H., Starikova, E., Sung, K., Tashkun, S.,  
1015 Tennyson, J., Toon, G. C., Tyuterev, V. G., and Wagner, G.: The HITRAN2012 molecular spectroscopic  
1016 database, *Journal of Quantitative Spectroscopy and Radiative Transfer*, 130, 4-50, 2013.
- 1017 Ryter, S. W. and Choi, A. M. K.: Carbon monoxide in exhaled breath testing and therapeutics, *J Breath*  
1018 *Res*, 7, 2013.
- 1019 Satar, E., Berhanu, T. A., Brunner, D., Henne, S., and Leuenberger, M.: Continuous CO<sub>2</sub>/CH<sub>4</sub>/CO  
1020 measurements (2012–2014) at Beromünster tall tower station in Switzerland, *Biogeosciences*, 13,  
1021 2623-2635, 2016.
- 1022 Severinghaus, J. P.: Studies of the terrestrial O<sub>2</sub> and carbon cycles in sand dune gases and in  
1023 Biosphere Doctoral Ph.D., Columbia University, New York, USA, 1995.
- 1024 Steig, E. J., Gkinis, V., Schauer, A. J., Schoenemann, S. W., Samek, K., Hoffnagle, J., Dennis, K. J., and  
1025 Tan, S. M.: Calibrated high-precision <sup>17</sup>O-excess measurements using cavity ring-down  
1026 spectroscopy with laser-current-tuned cavity resonance, *Atmos. Meas. Tech.*, 7, 2014.
- 1027 Stephens, B. B., Bakwin, P. S., Tans, P. P., Teclaw, R. M., and Baumann, D. D.: Application of a  
1028 differential fuel-cell analyzer for measuring atmospheric oxygen variations, *J Atmos Ocean Tech*, 24,  
1029 82-94, 2007.
- 1030 Tennyson, J., Bernath, P. F., Campargue, A., Császár, A. G., Daumont, L., Gamache, R. R., Hodges, J. T.,  
1031 Lisak, D., Naumenko, O. V., Rothman, L. S., Tran, H., Zobov, N. F., Buldyreva, J., Boone, C. D., De Vizia,  
1032 M. D., Gianfrani, L., Hartmann, J.-M., McPheat, R., Weidmann, D., Murray, J., Ngo, N. H., and



- 1033 Polyansky, O. L.: Recommended isolated-line profile for representing high-resolution spectroscopic  
1034 transitions (IUPAC Technical Report), 86, 1931–1943, 2014.
- 1035 Tohjima, Y.: Method for measuring changes in the atmospheric O-2/N-2 ratio by a gas  
1036 chromatograph equipped with a thermal conductivity detector, *J Geophys Res-Atmos*, 105, 14575-  
1037 14584, 2000.
- 1038 Valentino, F. L., Leuenberger, M., Uglietti, C., and Sturm, P.: Measurements and trend analysis of O<sub>2</sub>,  
1039 CO<sub>2</sub> and δ<sup>13</sup>C of CO<sub>2</sub> from the high altitude research station Junfgraujoch, Switzerland — A  
1040 comparison with the observations from the remote site Puy de Dôme, France, *Sci Total Environ*, 391,  
1041 203-210, 2008.
- 1042 Varghese, P. L. and Hanson, R. K.: Collisional narrowing effects on spectral line shapes measured at  
1043 high resolution, *Appl. Opt.*, 23, 2376-2385, 1984.
- 1044 Wójtewicz, S., Cygan, A., Masłowski, P., Domysławska, J., Wcisło, P., Zaborowski, M., Lisak, D.,  
1045 Trawiński, R. S., and Ciuryło, R.: Spectral line-shapes of oxygen B-band transitions measured with  
1046 cavity ring-down spectroscopy, *Journal of Physics: Conference Series*, 548, 012028, 2014.
- 1047 Wolf, P. G., Parthasarathy, G., Chen, J., O'Connor, H. M., Chia, N., Bharucha, A. E., and Gaskins, H. R.:  
1048 Assessing the colonic microbiome, hydrogenogenic and hydrogenotrophic genes, transit and breath  
1049 methane in constipation, *Neurogastroent Motil*, 29, 2017.
- 1050 Zellweger, C., Forrer, J., Hofer, P., Nyeki, S., Schwarzenbach, B., Weingartner, E., Ammann, M., and  
1051 Baltensperger, U.: Partitioning of reactive nitrogen (NO<sub>y</sub>) and dependence on  
1052 meteorological conditions in the lower free troposphere, *Atmos. Chem. Phys.*, 3, 779-796, 2003.
- 1053